INFN/AExxx, LAL 13-01, SLAC-R-xxx

Super*B* Detector Technical Design Report

Abstract

This report describes the technical design detector for Super*B*.

Contents

1 Drift Chamber

1.1 Overview

The Super$B$ Drift Chamber (DCH) is the main tracking detector of the Super$B$ experiment. Immersed in a 1.5 T solenoidal magnetic field, the DCH provides several position measurements along the track for a precise reconstruction of the particle momentum. It also measures the ionization energy loss used for particle identification. In fact, the DCH is the primary device in Super$B$ to measure velocities of particles having momenta below approximately 700 MeV/c and, at least in the initial phase of the experiment when no forward PID device is foreseen, it is the the only particle identification device for tracks with $\vartheta \leq 25°$.

Finally the drift chamber, together with the electromagnetic calorimeter, will provide the trigger of the experiment (see sec. **??**).

1.1.1 Physics Requirements

Similarly to *BABAR*, one of the goals of the Super$B$ experiment is to reconstruct exclusive and inclusive final states with high and well-controlled efficiency. This requirement implies maximal solid angle coverage and highly efficient reconstruction of tracks with $p_\perp$ as low as 100 MeV/c (the minimum transverse momentum of a track produced at the interaction point to leave enough hits in the drift chamber for being reconstructed).

Background rejection requires excellent momentum resolution over the full momentum spectrum. In *BABAR* the momentum resolution has been measured on muon tracks [1] to be $\sigma_{p_\perp}/p_\perp = (0.13 p_\perp + 0.45)\%$. In the Super$B$ drift chamber we aim at obtaining a similar, or better, result.

The average charged particle momentum in Super$B$ is less than 1 GeV/c, smaller than in *BABAR* due to the reduced boost. Multiple scattering will therefore be the main limiting factor to track parameter resolution for the majority of charged tracks in Super$B$. The effect is controlled by keeping to a minimum the material budget in the DCH. A thin inner wall helps matching tracks reconstructed inside the vertex detector with those in the DCH and improves the $p_\perp$ and the ϑ resolution by effectively increasing the lever arm of the tracking system when adding high precision measurement points from the vertex detector. It also reduces photon conversion thus minimising background in the chamber. Low-mass endplates and outer wall also limit photon conversions and multiple scattering which could degrade the performance of the detectors surrounding the DCH.

Finally, although the track dip angle is measured with high precision by the vertex detector, the DCH must provide an independent measurement of this angle to allow the reconstruction of secondary vertices of long-lived particles decaying outside the vertex detector region, as K^0_S mesons or Λ baryons. The DCH must also provide a measurement of the hit z coordinate. A stand-alone full 3D tracking in the DCH also helps in extrapolating tracks to the calorimeter, to the FDIRC detector and back to the vertex tracker, and allows their use in the L1 trigger.

1.1.2 Design Overview

The physics requirements outlined in the previous section can be met with a cylindrical drift chamber with performance similar to the *BABAR* one. We have therefore taken the *BABAR* drift chamber as a starting point, seeking improvements in two main areas: reduction of the detector material and improvement of the $\mathrm{d}E/\mathrm{d}x$ measurement.

We shall show that the first goal can be met with the adoption of modern construction techniques for the mechanical structure involving the

use of composite materials (Sec. 1.3), together with the use lighter gas mixtures and reduced wire material (Sec. 1.2). Improvements in the energy loss measurements could be achieved by adopting the Cluster Counting technique for the DCH readout. These two solutions constitute the baseline of the present design and will be discussed in detail in the remaining sections of this chapter.

We note that a fallback solution for the readout is represented by the standard TDC/ADC readout chain discussed in Sect.1.4.2.

To reach its ambitious goal on the integrated luminosity, the Super$B$ experiment will work in "factory-mode", taking data continously over extended run periods. This poses stringent requirements on the reliability of all its subdetectors, including the DCH. The *BABAR* drift chamber already met these requirements, and we expect that our choice of separating the signal digitization electronics from the on-detector preamplification boards will further improve the system reliability.

1.1.3 Geometrical Constraints

A side view of the drift chamber is shown in Fig. 1.1. The DCH inner radius is constrained by the final focus cooling system, by the Tungsten shield surrounding it and by the SVT service space to $R_{inner} = 270\,\text{mm}$. The outer radius is constrained to $R_{outer} = 809\,\text{mm}$ by the DIRC quartz bars, as in *BABAR*. The total length available for the DCH is $L = 3092\,\text{mm}$, including the space for front-end electronics, signal and high voltage cables, and the needed services (*e.g.* cooling, gas pipes). The space necessary for possible future upgrades of the Super$B$ detector such as the backward electromagnetic calorimeter (Section **????**) and the forward PID system (Section **??**) has already been taken into account.

As the rest of the detector, the drift chamber is shifted with respect to the interaction point by an offset, optimized for the DCH to be 333 mm (see Fig. 1.1).

1.1.4 Machine Background Considerations

Background processes are responsible for the largest part of the DCH rate. A rate higher than the design level would affect the charged track reconstruction, due to spurious hits, and generally degrade tracking performance. Additionally, the DAQ electronics can be progressively damaged when being exposed to a significant rate of particle for a long period of time. In both cases, an accurate simulation of the radiation rates is needed to estimate the real performances and the life-span of the electronics.

The main tool used to perform this estimate is the full simulation program described in detail in Sec. **??**. The chamber gas volume is described as an homogeneous medium with a density corresponding to the weighed average of the gas and the wires densities. The chamber structure is instead accurately described including carbon fiber inner and outer walls and endcaps, each with the appropriate density. Three silicon plates are included on the backwards side to simulate the amount of material corresponding to the front-end electronics. The basic information in the simulation output corresponds to a single interaction (or step) of the particle simulated by GEANT4. Each particle step inside the gas volume and silicon plates is recorded, together with additional information about the type of particle, its position, incident energy, vector momentum, and deposited energy. The simulation is not aware of the internal wire structure: this allows us to simulates background events faster, and rates can be computed in each layer for different wire configurations in a post-simulation analysis, as described below. The post-simulation analysis evaluates also the radiation dose, the equivalent fluence of 1 MeV neutrons, and fluences of different kind of particles in the plates representing the DAQ electronics.

A dedicated application has been developed to analyze the simulation output and produce the relevant quantities and plots. A given wire structure is provided as input to the application, with all the information on the cell size

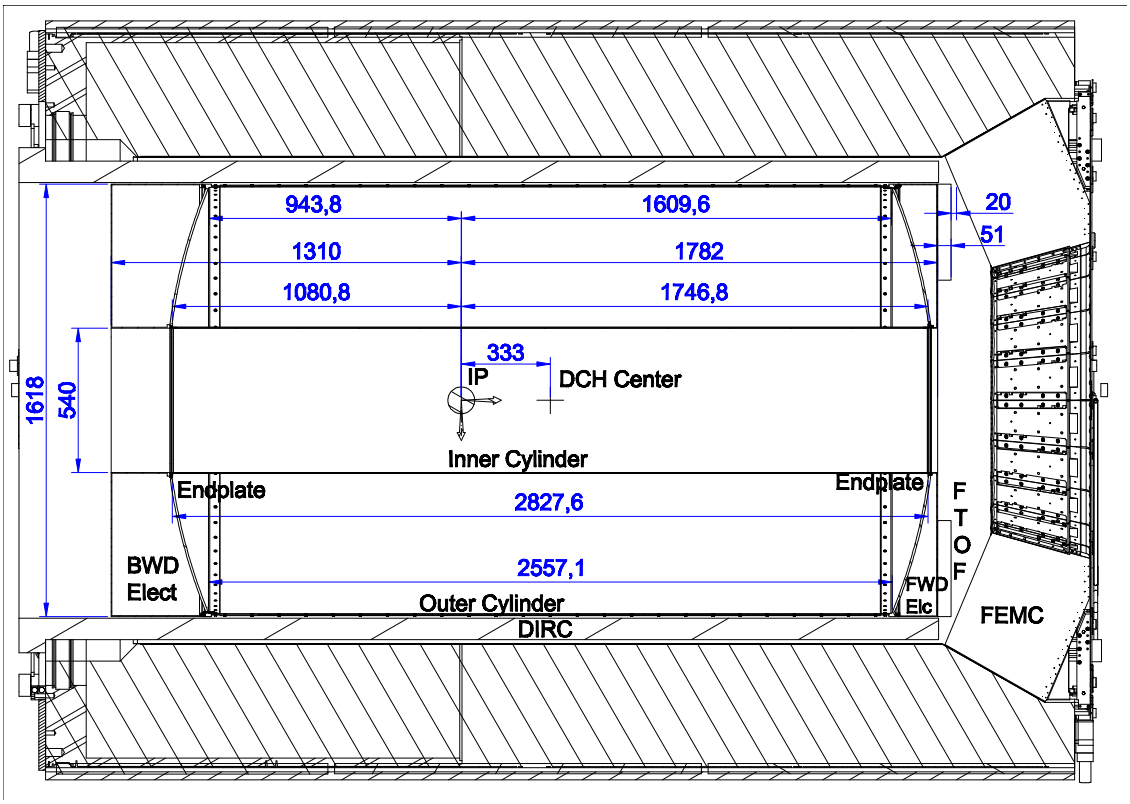

Figure 1.1: Longitudinal section of the DCH with principal dimensions.

and stereo angles. Given the long path, charged tracks curvature in the solenoidal magnetic field cannot be neglected. For each charged track crossing the gas chamber, the helix parameters are computed and the deposited energy in each crossed cell is added to a table where the deposited energy is stored for each cell. After having analyzed all the steps from charged tracks in the event, the table is used to fill a histogram with one entry for each layer: the number of cells with deposited energy greater than zero in each layer is added into the corresponding interval. A histogram is produced for all the background sources and then rescaled for the cross-section/frequency of each process. For each given transverse radius of the DCH, the tracks produced by background processes are with good approximation isotropic in azimuthal angle, so no information is lost when averaging the cells fired over the same layer.

The largest contributions to the rate are from radiative Bhabha and Pair productions. The simulation includes also contribution from Touschek scattering and beam scattering with residual gas. Photons from synchrotron radiation give a negligible contribution to the DCH rate and radiation levels, so they are omitted in the following. Figure 1.2 shows the total rate and the separate contribution for each background source assuming a typical configuration with axial cells only. Most of the background activity is located around the interaction point, so the rate decreases fast when moving to outer layers. No significant difference in the shape of the rate is observed between different background sources, because most of the particles that hit the chamber are not primaries, but particles that exit the final focus shielding after many interactions, as explained below.

We found that the DCH rate had a significant dependence on the maximum step length

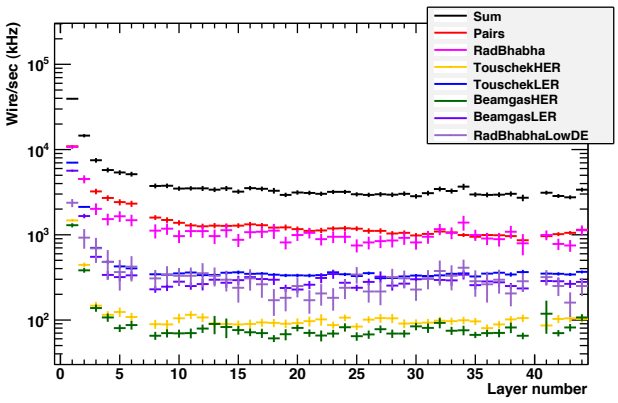

Figure 1.2: Total rate for each DCH layers for a typical axial configuration. The empty intervals correspond to emty spaces between groups of layers. The separate contributions from each background source are also showed using different colors (color online, see Table **??** for more details on the samples).

allowed in the GEANT4 simulation. A dedicated study showed that this is due to a poor simulation of the multiple scattering over long distances in low density materials. For this reason the maximum step length in the gas chamber has been fixed to 1 mm, reducing this dependence to a negligible level.

The studies showed that the largest part of the rate is not due to charged tracks coming directly from the interaction point, but mostly from photons coming out of the shielding and kicking out electrons off the chamber walls when they enter the chamber. Looking specifically at those photons coming out of the final focus elements, we were able to detect some areas where the number of particles was higher than usual. The shielding has been subsequently optimized to reduce the number particles from those areas.

Photons impinging on the DCH wall produce low energy electrons that can still travel long distances in the gas. If their transverse momentum is small, they can even traverse the whole chamber spiralizing along the z coordinate. In the case of stereo layers, one such a particle travelling along the longitudinal direction can thus cross multiple cells, explaining the higher rate observed in the stereo layers shown in Fig. 1.3. The wires in the central block from layer 11 to

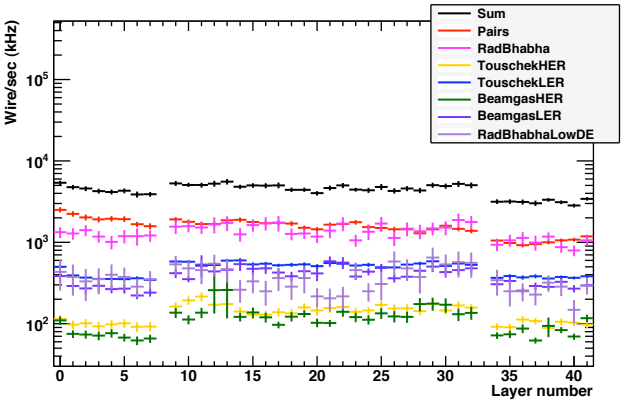

Figure 1.3: Total rate for each DCH layers for a typical stereo configuration (layer 11-34, stereo angle of 70-90 mrad). The empty intervals correspond to emty spaces between groups of layers. The separate contributions from each background source are also showed using different colors (color online, see Table **??** for more details on the samples).

34 have a stereo angle from 70 to 90 mrad, and show clearly a rate higher than the neighbour axial wires. The higher rate in the first layers observed in the plot of Fig. 1.2, is not present here because, for this configuration, the first layer is 2 cm far from the inner wall.

With the geometry used for the simulation, a typical configuration with a central section of stereo layers, and an integration time of 1μs, the occupancy is estimated at $\sim 5\%$.

The radiation levels estimated in the region where the electronics will be located are generally low. For a period corresponding to an integrated luminosity of 10 ab^{-1} the estimated dose is below 8 Gy, the equivalent 1 MeV neutron fluence is below 3×10^{11} $n_{eq}/cm^2/yr$, and the fluence due to hadrons with kinetic energy larger than 20 MeV is below 7×10^{10} $n_{eq}/cm^2/yr$.

1.2 Design Optimization

The *BABAR* drift chamber operational record has been quite good, both for what performances and reliability is concerned. For this reason, several features of the Super$B$ DCH, which will operate in a similar environment, derive from the *BABAR* drift chamber.

Nevertheless, over fifteen years after its design and construction, we have looked for possible design improvements to build a drift chamber with performances yet better that the *BABAR* one.

1.2.1 Performance Studies

We have made extensive simulation studies to evaluate the impact on track reconstruction of a number of design choices concerning both the external structure (radius and material of the inner cylynder, position and shape of the endplates) and the internal layout (cell shape, wire orientation). The studies have been performed using the Super$B$ fast simulation tool *FastSim*, whose main features are described in Chapter **??**. The main results of these studies are summarised in the following sections.

1.2.1.1 Radius and Thickness of the Inner Wall

The simulation of several signal samples with both high (*e.g.* $B \to \pi^+\pi^-$), and medium-low (*e.g.* $B^0 \to D^{*-}K^+$) momentum tracks indicates that, as expected, the momentum resolution improves as the minimum drift chamber radius R_{min} decreases, as long as the hit rate per layer is low enough not to significantly impact the reconstruction. However, as discussed in Sect. 1.1.3, R_{min} is actually limited by mechanical constraints from the cryostats and radiation shields, and is set to $R_{min} = 270$ mm.

The thickness of the inner wall can affect significantly the reconstruction of charged particles, especially those with lower momentum where multiple scattering is larger. For example, the width of the ΔE distribution in $B^0 \to D^{*-}K^+$ events gets about 7% narrower if the thickness of the carbon fiber inner wall is decreased from 1 mm — the value in *BABAR*, corresponding to 0.4% X_0 — to about 0.2 mm (0.1% X_0). A carbon fiber, 0.2 mm-thick inner cylinder is the current baseline, although an even thinner solution is being considered as discussed in Sect. 1.3.1.

1.2.1.2 Endcap shape and position

A study was carried out to compare the momentum and $\mathrm{d}E/\mathrm{d}x$ measurement resolution of tracks reconstructed in the forward or backward directions as a function of the endcap shape (convex or concave) and its position along the beam (z) axis. Fig. 1.4 shows two of these configurations together with the definition of the forward and backward regions.. We simulated samples of single charged pions with flat p and $\cos\theta$ distributions and samples of $B^0 \to D^{*-}K^+$ decays. We compared the $p_\perp$ resolution, the K/π separation based on $\mathrm{d}E/\mathrm{d}x$ and the reconstruction efficiency of $B^0 \to D^{*-}K^+$ for different configurations. At fixed z position, the average $p_\perp$ resolutions for the concave and convex shapes are consistent within a 3% relative uncertainty in both the forward and backward

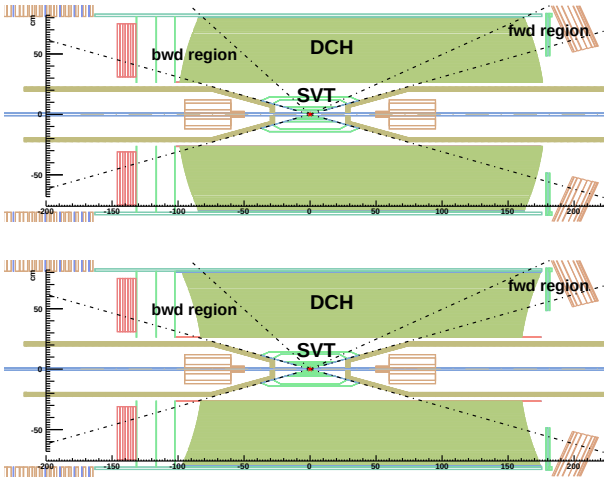

Figure 1.4: Example of DCH configurations where the endcaps are placed in the same position (same z_{min} and z_{max}) but their shape is different: convex (top) and concave (bottom). The forward and backward regions are indicated.

regions. The average K/π separations are also consistent within 1-2%. Differences of this order of magnitude depend on the specific polar angle distribution of the tracks. The reconstruction efficiency of $B^0 \to D^{*-}K^+$ events is not affected by the endcap shape in the forward region, while it is slightly higher ($\approx 1\%$) when the endcap in the backward region is convex. The average variation of $\sigma(p_\perp)/p_\perp$ as a function of the endcap position is roughly consistent with 1% (1.5-2.0%) per additional cm of DCH length in the forward (backward) direction. Similarly, the average K/π separation based on $\mathrm{d}E/\mathrm{d}x$ increases by about 0.5% (1%) per additional cm of DCH length in the forward (backward) region. This asymmetry between the forward and backward direction is ascribed to the different average number of crossed layers.

To summarize, also as a result of weighing the effects discussed above for the fraction of tracks crossing these regions (typically below 10% of the total), little difference in terms of performance is observed between the concave and convex endplate shapes *per se*, while the length does have a significant impact. Due to the details of mechanical design of the endplate outer flanges, convex endplates allow for a longer DCH.

1.2.1.3 Wire and Gas Material

The *BABAR* drift chamber featured concentric layers of hexagonal cells, organized in axial (A), positive stereo (U) or negative stereo (V) superlayers. This choice was motivated by the good symmetry of the hexagonal cells, and by the small number of field wires per sense wire (field-to-sense wire ratio $\mathcal{R}_{f:s} = 2$) because many field wires are shared among adjacent cells. However, such a small value $\mathcal{R}_{f:s}$ required larger wire diameters –therefore more material in the tracking volume and more force on the endplates – to avoid gas amplication at the field wires. In addition, the advantage of stringing fewer field wires was outbalanced by the guard wire layers needed at every super-layer transition to keep the electric field homogeneous across layers (hexagonal cells with different stereo angles cannot intersect radially and must be separated). In Table 1.1 we report the material budget for the hexagonal *BABAR*-like layout and for two alternative solutions using rectangular cell geometry with different values for $\mathcal{R}_{f:s}$. All the numbers shown in Table 1.1 and used in the simulations below were obtained for an inner DCH radius of $R_{min} = 210$ mm and a cell height of 12 mm (the final configuration will have cells of slightly different heights, as discussed in Sec. 1.2.3). The case in which the field Aluminum wires are coated with a 0.5 μm thick gold plating is compared to the case where the coating is absent. Since in the square cell configurations there is no need to leave space between superlayers with different stereo orientation, for a given cell size it is possible to allocate more measurement layers compared to the hexagonal configuration. The average single hit spatial resolutions are estimated to be similar in all configurations. Fig. 1.5 compares $\sigma(p_\perp)/p_\perp$ vs $p_\perp$ for the configurations in Tab. 1.1. The average $p_\perp$ resolution in the $\mathcal{R}_{f:s}$=4 square cell configuration is about 5% better than in the hexagonal cell scenario.

Table 1.1: Combined gas+wires material budget for different cell geometries in a $80\%\mathrm{He} - 20\% i\mathrm{C_4H_{10}}$ mixture. Values from the *BABAR* DCH are shown in boldface.

Cell layout	$\rho(g/cm^3)$ $\times 10^4$	X_0 (m)	# layers
	coat/nocoat	coat/nocoat	
Hex 2:1	**10.0**/9.5	**270**/350	40
Sqr 3:1	9.8/8.5	310/400	44
Sqr 4:1	8.5/8.1	320/430	44

The effect of the material budget of different gas mixtures was also studied. We considered square cell configurations with $\mathcal{R}_{f:s}$=3 and threes gas mixtures: He80-Ibu20, He90-Ibu10 and He80-Met20. Fig. 1.6 shows $\sigma(p_\perp)/p_\perp$ vs $p_\perp$ for the three scenarios. $\sigma(p_\perp)/p_\perp$ for the He80-Ibu20 configuration is 10-15% worse than in the He80-Met20 mixture.

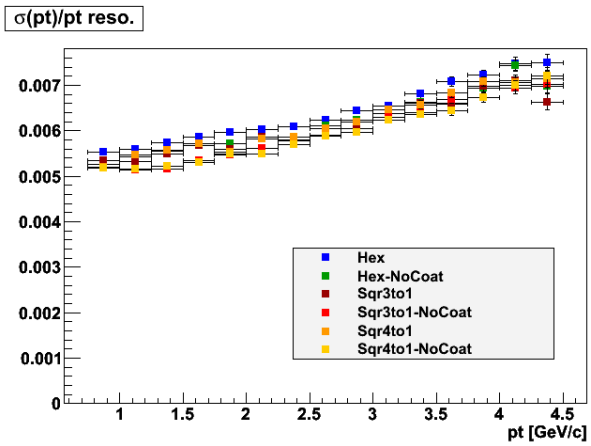

Figure 1.5: Relative $p_\perp$ resolution for different cell geometries. The color codes refer to the configurations in Table 1.1.

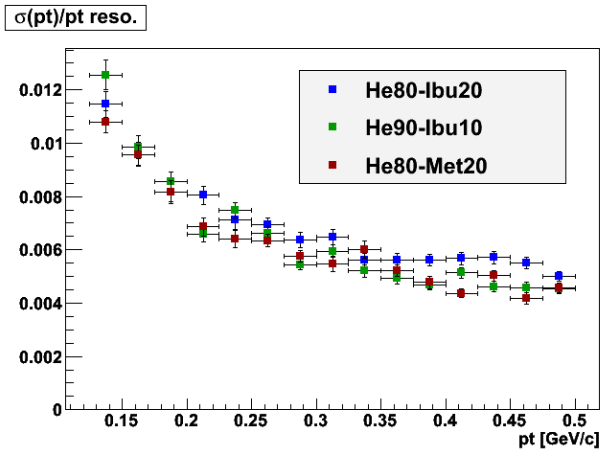

Figure 1.6: Relative $p_\perp$ resolution for different gas mixtures in the configuration with rectangular cells and $\mathcal{R}_{f:s} = 3$.

1.2.1.4 Stereo Angle Layout

The impact of the stereo angle layout on tracking performance was studied by comparing the reconstruction of $B \to \pi^+\pi^-$ and $B \to D^*K$ events in four different configurations: *i)* a *BABAR*-like AUVAUVAUVAUVA; *ii)* a completely axial DCH; *iii)* a "mostly stereo SL" layout in which the innermost and outermost superlayers are axial, and the remaining ones alternate positive and negative stereo orientations, AUVUVUVUVA; and *iv)* a "stereo layers" configuration in which two axial superlayers placed in the innermost and outermost position surround a set of alternate stereo angle layers (alternate stereo angle layers were *e.g.* used in the KLOE drift chamber). The outcome of this study is that since the Silicon Vertex Tracker largely dominates the polar angle measurement, the arrangement of the stereo layers does not impose tight constraints on tracking: for example both the $p_\perp$ and the ΔE resolution are almost identical in the four configurations (configuration *iii)* is slightly better for the case of relatively softer tracks in $B \to D^*K$ events). Compared to the completely axial configuration, however, configurations with stereo layers are preferred because they can provide – in addition to 3D trigger information – some constraints on the polar direction of those few tracks that are not reconstructed in the SVT.

1.2.2 Cluster Counting

A possibility being considered to improve the performances of the gas tracker is the use of the cluster counting method. Signals in drift chambers are usually split to an analog chain which integrates the charge, and to a digital chain recording the arrival time of the first electron, discriminated with a given threshold. The cluster counting technique consists instead in digitizing the full waveform to count and measure the time of all individual peaks. On the assumption that these peaks can be associated to the primary ionization acts along the track, the energy loss and to some extent the spatial coordinate measurements can be substantially improved. In counting the individual cluster, one

indeed removes the sensitivity of the specific energy loss measurement to fluctuations in the amplification gain and in the number of electrons produced in each cluster, fluctuations which significantly limit the intrinsic resolution of conventional $\mathrm{d}E/\mathrm{d}x$ measurements.

The ability to count the individual ionization clusters and measure their drift times strongly depends on the average time separation between them, which is, in general, relatively large in He-based gas mixtures thanks to their low primary yield and slow drift velocity. Other requirements for efficient cluster conting include good signal-to noise ratio but no or limited gas-gain saturation, high preamplifier bandwidth, and digitization of the signal with a sampling speed of the order of 1Gs/sec. Finally, it is necessary to extract online the relevant signal features (*i.e.* the cluster times), because the DAQ system of the experiment would hardly be able to manage the enormous amount of data from the digitized waveforms of the about 10 000 drift chamber channels.

1.2.3 Cell Design and Layer Arrangement

The cell must be designed to optimise the homogeneity of the electric field inside it; this is particularly relevant with the non-saturated mixture we intend to use. Other critical parameters are the wire material and an optimal use of the drift chamber volume for accommodating as many measurament points as possible.

The design for the Super$B$ drift chamber employs small rectangular cells arranged in concentric layers about the axis of the chamber. The z coordinate of the track hits is measured by orienting a subset of the wire layers at a small positive or negative stereo angle, ε, relative to the chamber axis. Such a measurement is performed with precision $\sigma_z \simeq \sigma_{R\phi}/\tan\varepsilon$. As in *BABAR*, four consecutive cell layers are grouped radially into a superlayer (SL). This will allow to keep the same *BABAR* algorithms for track-segment finding, both in the track reconstruction and in the formation of the drift chamber trigger.

The rectangular cell layout ensures the most efficient filling of the drift chamber volume, because the transition between superlayers of opposite stereo angles does not require to leave free radial space, nor layers of field-shaping guard wires. Indeed, the latter are only used at a radius inside the innermost SL and at a radius outside the outermost SL. Such guard wires also serve the purpose to electrostatically contain very low momentum electrons produced from background particles showering in the DCH inner cylinder and in the SVT, or background-related backsplash from detector material just beyond the outer SL.

Simulations[2] have shown that a field:sense wire ratio of 3:1 ensures good homogeneity of the electric field inside the cells. In this configuration, used successully by previous experiments [3, 4], each sense wire is surrounded by 8 field wires.

The radial positions of the stereo wires in the j-th layer vary with the z coordinate, being larger at the endplates than at the center of the chamber by the "stereo drop" $\delta_j \equiv R_j^{\mathrm{EP}} - R_j$. The cell shapes are most uniform when $\delta_j = \delta$ is a constant for all layers: this is obtained by changing the stereo angle with the radius, by the relation $\tan\varepsilon_j = 2\delta/L_j\sqrt{2R_j^{\mathrm{EP}}/\delta - 1}$ (L_j is the chamber length at layer j).

Additional constraints used to determine the cell layout include:

a) the number of cells of width w_j on the j-th sense wire layer, $N_j = 2\pi R_j/w_j$, must be an integer number;

b) to keep a fixed periodicity in signal and high voltage distribution, it is convenient that the number of cells per layer is incremented of a fixed quantity ΔN when passing from a SL to the next one.

c) since the density of both physical tracks and background hits is higher at smaller radii, we choose to have smaller cells in the innermost layers of the drift chamber.

A possible choice for the drift chamber layout, obtained for $\delta = 8\,\mathrm{mm}$ and $\Delta N = 16$ is

shown in Table 1.2. In this arrangement the two innermost SL's contain 1472 cells with height $h = 10\,\text{mm}$ and widths $w = (10.2 \div 11.7)\,\text{mm}$. The cells in the remaining superlayers have $h = 12.85\,\text{mm}$ and $w = (16.1 \div 19.1)\,\text{mm}$. There are a total of 7872 cells in the drift chamber. The first two superlayers have an axial orientation; this minimizes the occupancy from background hits due to low-momentum spiraling electrons which traverse the drift chamber along its axis (see Sec.1.1.4). The two external superlayers are also axial. The fact that the innermost and outermost superlayers do not exhibit the stereo drop deformation δ matches the axial simmetry of the inner and outer drift chamber cylinders. The six internal SL's have a stereo arrangement, with angles as shown in the Table.

The corresponding wire map in the region with angle $|\varphi| < 10^\circ$ is shown in Fig. 1.7 at the center of the chamber (a) and at the endplates (b).

It is seen that the axial-stereo transition between SL 2 and SL 3 creates some additional radial space close to the endplates, which disappears at the DCH center. The opposite happens at the stereo-axial transition between SL 8 and SL 9. It is clear that the electric field should be as uniform as possible across layers to ease the drift chamber calibration; however, simulation studies have shown that the field distortion at the two transition radii is moderate and does not require to be compensated by layers of guard wires, which would add material and reduce the sensitive volume.

In Fig.1.8 we show the drift lines and the isochrone curves for two sample rectangular cells of the proposed Super$B$ drift chamber with a 90%He $-$ 10%iC$_4$H$_{10}$ gas mixture, in a 1.5 T magnetic field. The rectangular cells with field:sense wire ratio of 3:1 are indeed a satisfactory compromise, ensuring that the field lines are sufficiently contained within the cell and the isochrone lines are isotropic for most of the drift region, while at the same time the number of field wires is not excessively large.

Table 1.2: A possible drift chamber SL structure, specifying the number of cells per layer, the radius at the center of the chamber of the innermost sense wire layer in the SL, the cell widths, and wire stereo angles, which vary over the four layers in a SL as indicated.

SL	N_{cells}	R [mm]	width [mm]	Angle [mrad]
1	176	292.5	10.4 – 11.5	0
2	192	332.5	10.9 – 11.9	0
3	144	375.4	16.4 – 18.1	+(63 – 66)
4	160	426.8	16.8 – 18.3	−(67 – 69)
5	176	478.2	17.1 – 18.4	+(70 – 72)
6	192	529.6	17.3 – 18.6	−(73 – 75)
7	208	581.0	17.5 – 18.7	+(76 – 77)
8	224	632.4	17.7 – 18.8	−(78 – 79)
9	240	691.8	18.1 – 19.1	0
10	256	743.2	18.2 – 19.2	0

1.2.4 Gas Mixture

The gas mixture for the Super$B$ drift chamber is chosen to allow optimal resolution in the measurement of both momentum and energy loss. It must also be operationally stable (*e.g.*, have a wide high voltage plateau), and be little sensitive to photons with $E \leq 10\,\text{keV}$ to help controlling the rate of background hits (see Sec. 1.1.4). Finally, aging in the chamber should be slow enough to match the projected lifetime of a typical High Energy Physics experiment (about 15 years). These requirements already concurred to the definition of the *BABAR* drift chamber gas mixture (80%He $-$ 20%iC$_4$H$_{10}$). Indeed, a high Helium content reduces the gas density and thus the multiple scattering contribution to the momentum resolution. Good spatial resolution calls for high single electron efficiency and for small diffusion coefficient. The effective drift velocity in Helium-based gas mixtures is typically non saturated, therefore it depends on the local electric field, and on the Lorentz angle. This dependences can be taken into account by a proper calibration of

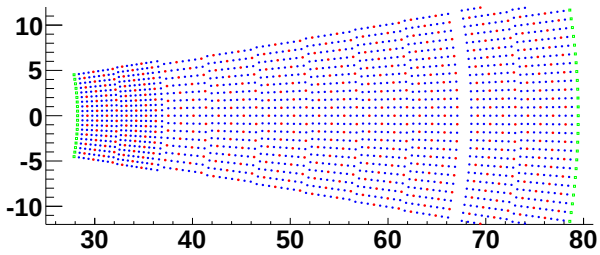

(a) Cell layout at the drift chamber center.

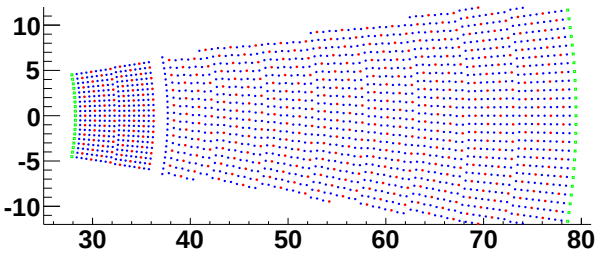

(b) Cell layout at the drift chamber endplates.

Figure 1.7: A possible cell layout of the Super$B$ drift chamber with $h_{\rm in} = 10\,\mathrm{mm}$, $h_{\rm out} = 12.85\,\mathrm{mm}$. Open green squares: guard wires; open blue circles: field wires; full red circles: sense wires. Note how the boundary regions after the first 8 layers of axially strung wires in the inner part of the chamber and after the following 24 layers of stereo layers map differently at the drift chamber center and at the endplates.

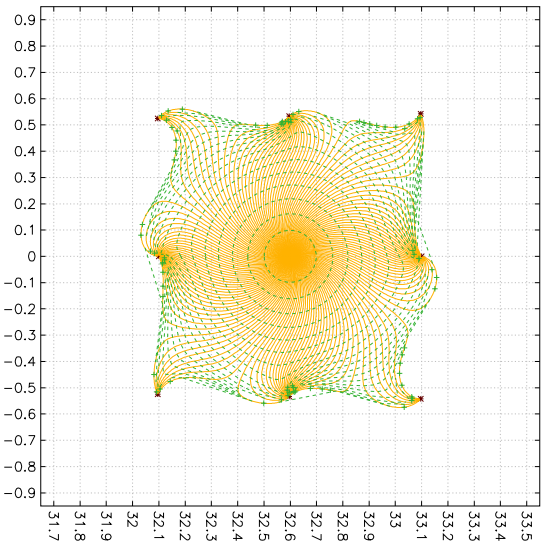

(a) Field and isochrone lines in a sample "small" cell, on layer n. 6.

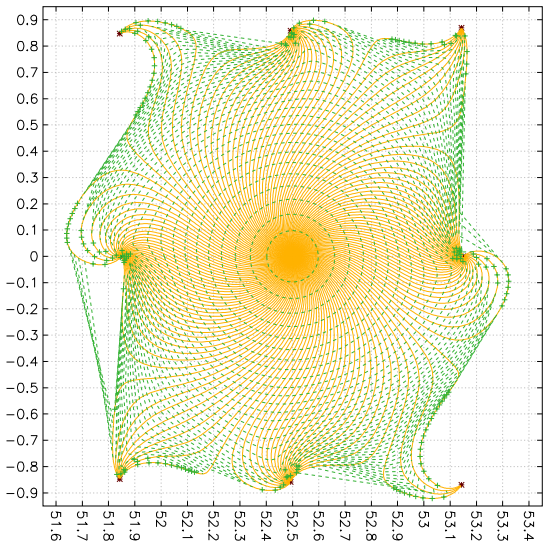

(b) Field and isochrone lines in a sample "big" cell, on layer n. 22.

Figure 1.8: Field lines and isochrone curves (shown with a 25 ns step) in a cell belonging to the first 8 layers (left) and in a larger cell of the outermost 32 layers (right).

Table 1.3: A possible drift chamber layer structure, specifying the number of cells per layer, the wire layer radius at the center of the chamber, the cell width and the wire stereo angle.

layer	N_{cells}	R [mm]	width [mm]	Angle [mrad]	layer	N_{cells}	R [mm]	width [mm]	Angle [mrad]
1	176	292.5	10.4	0.0	21	192	529.6	17.3	-67.7
2	176	302.5	10.8	0.0	22	192	542.4	17.7	-68.6
3	176	312.5	11.2	0.0	23	192	555.3	18.2	-69.6
4	176	322.5	11.5	0.0	24	192	568.1	18.6	-70.6
5	192	332.5	10.9	0.0	25	208	581.0	17.5	71.6
6	192	342.5	11.2	0.0	26	208	593.8	17.9	72.6
7	192	352.5	11.5	0.0	27	208	606.7	18.3	73.5
8	192	362.5	11.9	0.0	28	208	619.5	18.7	74.5
9	144	375.4	16.4	55.7	29	224	632.4	17.7	-75.5
10	144	388.2	16.9	56.7	30	224	645.2	18.1	-76.5
11	144	401.1	17.5	57.7	31	224	658.1	18.5	-77.5
12	144	413.9	18.1	58.7	32	224	670.9	18.8	-78.5
13	160	426.8	16.8	−59.7	33	240	691.8	18.1	0.0
14	160	439.6	17.3	−60.7	34	240	704.6	18.4	0.0
15	160	452.5	17.8	−61.7	35	240	717.5	18.8	0.0
16	160	465.3	18.3	−62.7	36	240	730.3	19.1	0.0
17	176	478.2	17.1	63.7	37	256	743.2	18.2	0.0
18	176	491.0	17.5	64.7	38	256	756.0	18.6	0.0
19	176	503.9	18.0	65.7	39	256	768.9	18.9	0.0
20	176	516.7	18.4	66.7	40	256	781.7	19.2	0.0

the space-time relations and in principle do not pose limits to attaining the required spatial resolution. In practice, a careful choice of the cell shape (see the dicussion in Sec. 1.2.3), and a small value of the Lorentz angle are an advantage.

To match the more stringent requirements on occupancy rates of Super$B$, it could be useful to select a gas mixture with a larger drift velocity in order to reduce ion collection times and so the probability of hits overlapping from unrelated events. The cluster counting option would instead call for a gas with low drift velocity and primary ionization. As detailed in Section1.2.5, R&D work is ongoing to optimize the gas mixture.

1.2.5 R&D and Prototype Studies

In order to optimize the gas mixture for the Super$B$ environment, and to asses both the feasibility and the operational improvements for the cluster counting technique a complete R&D program has been proposed. The program includes both beam tests and cosmic ray stands to monitor performancs of *ad hoc* built prototypes. While the dE/dx resolution gain of the cluster counting method is in principle quite sizeable compared to the traditional total charge collection, the actual capability of the measured number of cluster might not retain the same analyzing power, due to a pletora of experimental effects that should be studied in detail so that the energy loss measurement derating should be assessed and, if possible, cured.

A few prototypes were built and operated to answer the above mentioned questions.

1.2.5.1 Prototype 1

The first one is a small aluminum chamber, 40 cm long, with a geometry resembling the the original *BABAR* drift chamber. It consists of 24 hexagonal cells organized in six layers with four cells each. A frame of guard wires with appropriate high voltage settings surrounds the cell array to ensure uniformity of the electric field among the cells. The device was operated in a cosmic ray test stand in conjunction with an external telescope, used to extrapolate the track trajectories with a precision of 80 μm or better. Different gas mixtures have been tried in the prototype: starting with the original *BABAR* mixture (80%He-20%iC_4H_{10}) used as a calibration point, both different quencher proportions and different quenchers have been tested in order to assess the viability of lighter and possibly faster operating gases.

As an example, the correlation between the extrapolated drift distance and the measured drift time is shown in Fig. 1.9 for a 80%He-20%iC_4H_{10} gas mixture. The result of a fit to a 5^{th}-order Chebychev polynomial is superimposed to the experimental points. Track-fit residuals and spatial resolution as a function of the drift distance for the same gas mixture are show in Fig. 1.10.

1.2.5.2 Prototype 2

A full-length drift chamber prototype was designed, built and commissioned to study cluster counting in a realistic environment, including signal distortion and attenuation along 2.5 meter long wires. The prototype, which is also meant to serve as a test bench for the final Front-End electronics and for the drift chamber trigger, is composed by 28 square cells with 1.4 cm side, arranged in eight layers and – as in the final Super$B$ drift chamber – with a field-to-sense wire ratio of 3:1. The eight layers have either 3 or 4 cells each, and are staggered by half a cell side to help reduce the left-right ambiguity. Tracks with angle $|\vartheta| \leq \pm 20°$ cross all the eight layers of the chamber. A set of guard wires surrounds the matrix of 28 cells to obtain a well-behaved field distribution at the boundary of the active detector volume. Most of the cells feature a 25 μm Gold-plated Molybdenum sense wire, while for

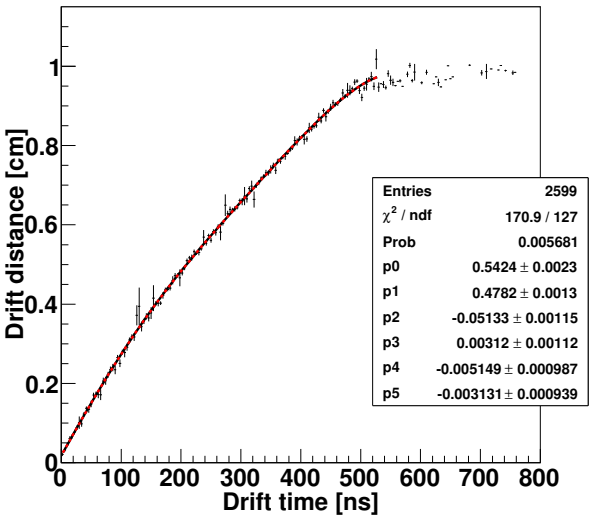

Figure 1.9: Track distance vs. drift time in a cell of the prototype. The line is the result of a fit with a 5^{th}-order Chebychev polynomial.

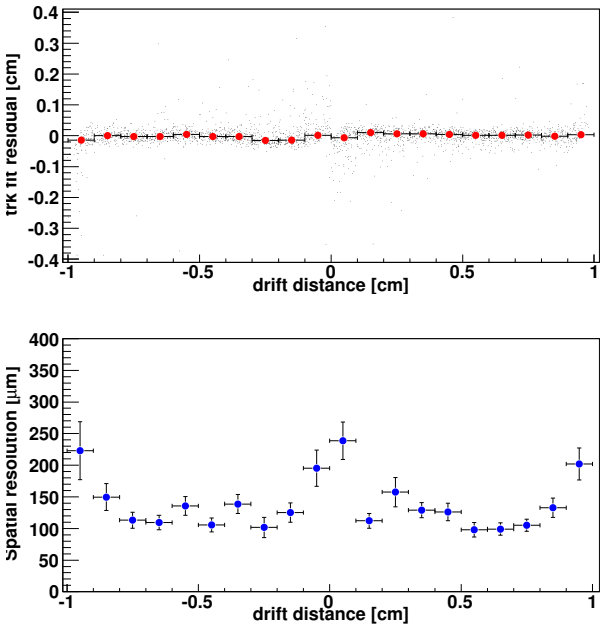

Figure 1.10: Track fit residuals (top) and spatial resolution (bottom) as a function of the drift distance.

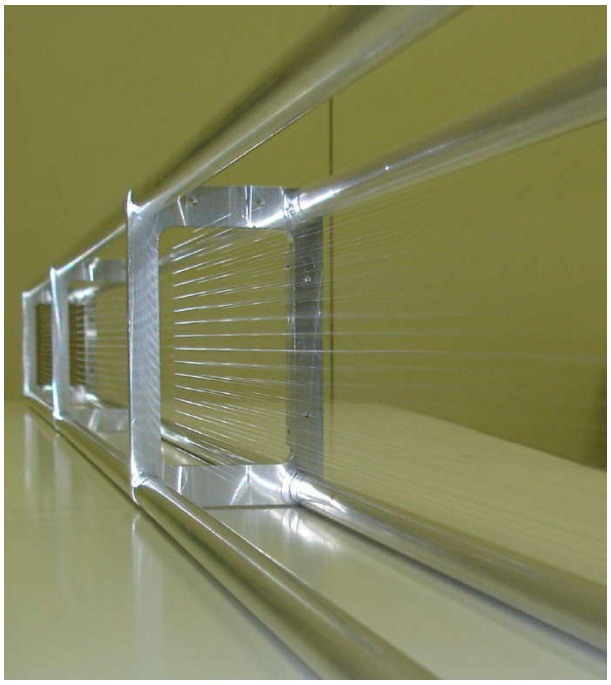

Figure 1.11: Prototype 2: detail of the strung wires.

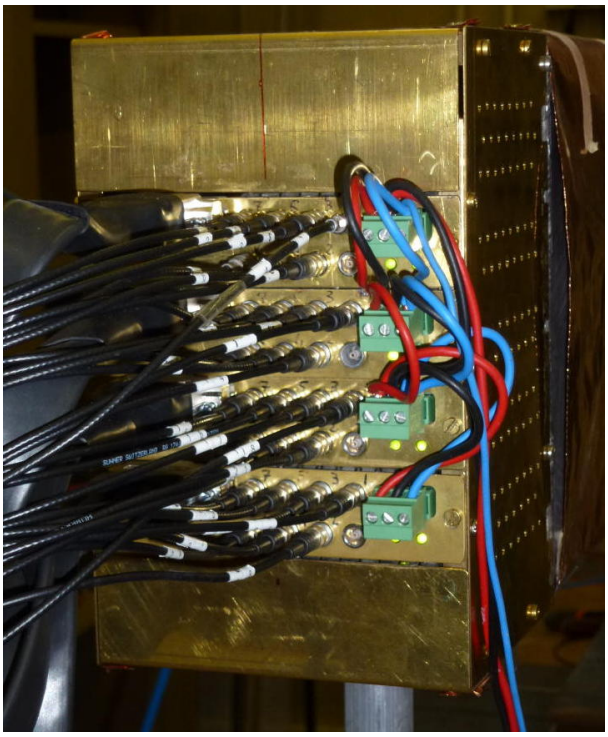

Figure 1.12: Prototype 2: FEE Faraday cage with signal and trigger cables.

reference seven cells in two adjacent layers are strung with a 25 μm Gold-plated Tungsten wire, traditionally used in drift chambers. The reason for using the Molybdenum wire is its lower resistivity, therefore smaller dispersion for pulses travelling along the wires. A picture of the chamber after stringing completion is shown in Fig. 1.11. The entire wire structure is enclosed in an Aluminum container 3 mm thick; three pairs of thin windows have been carved in the middle and at the extremities in order to have smaller amount of material in the path of low energy particles measured by the device. Four preamplifier boards are used to extract the cell signals. Each board serves seven channels, each with a transimpedence preamplifier (rise time of about 2.4ns), at a nominal gain of 8mV/fC and a noise of 2200 e rms. Each boards also has a test input, both unipolar and differential outputs (50 Ω– 110 Ω); the latter are used for a test implementation of the Drift Chamber first level trigger. A detail of the Faraday cage housing the FEE boards and of the signal and trigger cables is shown in Fig. 1.12.

The data collected with this prototype are fed into a switch capacitor array digitizer[1], which samples the wire signals at 1 GS/sec with and input BW$\geq$ 500 MHz. The challenge of detecting the ionization clusters in signals with a wide dynamic range and non-zero noise levels is apparent from the two sample waveforms shown in Figg. 1.13, recorded in the cosmic-ray setup. Hits associated to cosmic ray tracks reconstructed in the drift chamber prototype are used to compare the performances in the energy loss measurement of the traditional truncated mean algorithm and of the cluster counting method. Preliminary results when 10 samples from a single prototype cell are used to form a 70% truncated mean or to count the average number of clusters are shown in Fig. 1.14. In the experimental conditions of our test, cluster

[1] CAEN V1742: http://www.caen.it/csite/CaenProfList.jsp?parent=13&Type=WOCateg

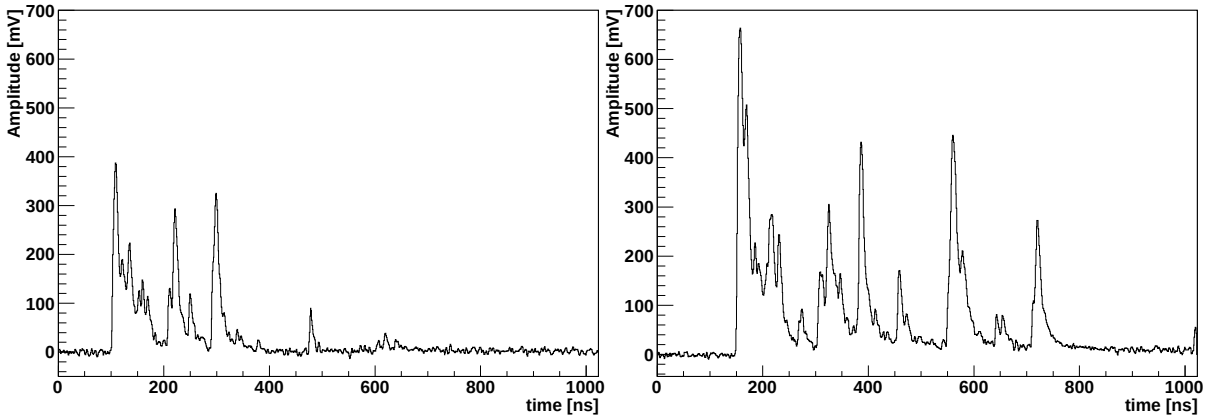

(a) Sample waveform n.1 (b) Sample waveform n.2

Figure 1.13: Sample waveforms from two cells of the full-length drift chamber prototype.

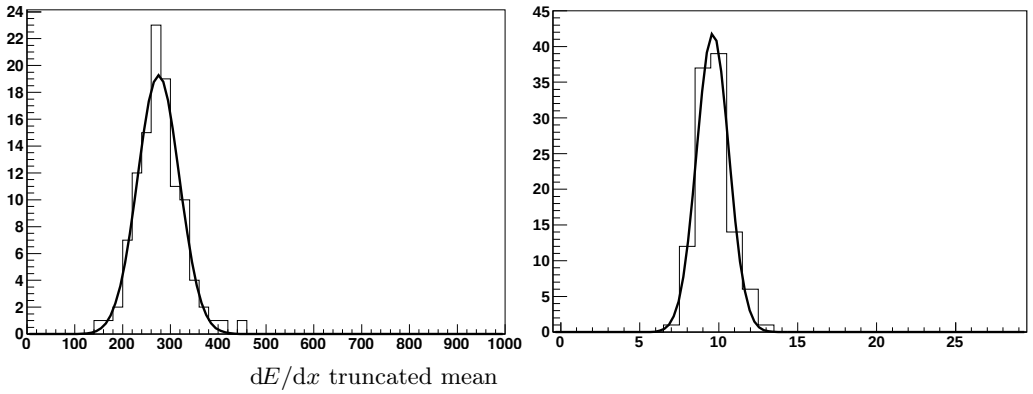

(a) Average dE/dx distribution (b) Average n. of clusters

Figure 1.14: Average dE/dx and number of clusters from 10 samples of a single cell belonging to a track reconstructed in the prototype.

counting yields a 40-50% better relative resolution than the truncated mean method. Additional R&D efforts are ongoing to extend this encouraging result to different momentum regions, and study how the $K-\pi$ resolving power in the range of interest of Super$B$ ($|p| \leq 5\,\mathrm{GeV}/c$) improves with the cluster counting technique.

The spatial resolution measured in the rectangular cells of the prototype operated in a 90%He-10%iC_4H_{10} gas mixture is shown in Fig. 1.15 as a function of the drift distance.

1.2.5.3 Single Cell Prototypes

Two beam tests of single-cell drift chamber prototypes have been carried out at the TRIUMF M11 beam line. The goals of the tests were:

- to establish the benefits of clusters counting for particle identification;
- to study the suitability for cluster counting of various amplifier prototypes provided by the University of Montreal; and
- to quantify the impact on particle identification performance of various design choices, including sense wire diameter, cable for transmitting the analog signal, connectors, termination, and gas gain.

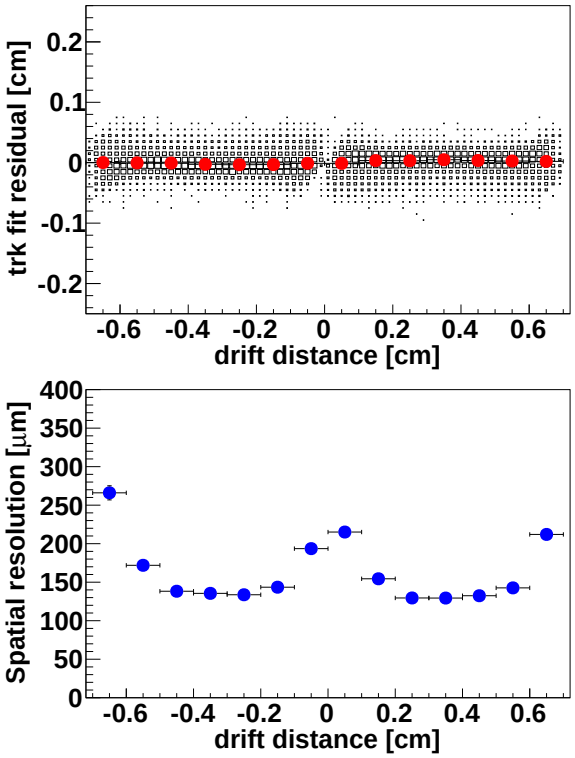

Figure 1.15: Track fit residuals (top) and spatial resolution (bottom) as a function of the drift distance in the rectangular cells of prototype 2 operated in a 90%He-10%iC_4H_{10} gas mixture.

The beam test in November 2011 used a single prototype, with 25 μm diameter sense wire, while the test in summer 2012 used two prototypes, one with 20 μm sense wire, and the other with either 25 or 30 μm. The prototypes were 2.7m long, and consisted of a single 15 mm square cell surrounded by an array of bias wires that adjusted the electric field distribution within the cell to be that expected for a large drift chamber [Fig. 1.16]. A 90% helium / 10% isobutane (90:10) mixture was used for the summer 2012 tests, while the November 2011 test also tested 80:20 and 95:5.

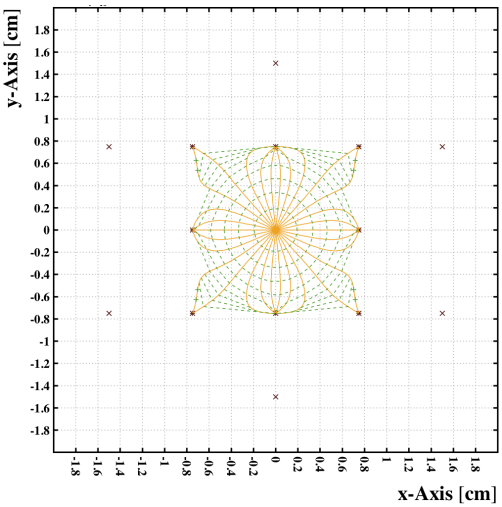

Figure 1.16: Cell design of the single cell prototypes.

Five different amplifier prototypes were built for the test, with three different input impedances: 50, 170, and 380Ω. The impedance of the cell is 380Ω, and for most tests, the cell was terminated at this value on the non-readout end. The 170 and 380Ω consisted of an impedance-matching front end, followed by a

100× gain stage (of 50Ω input impedance); the 50Ω amplifier consisted only of this gain stage.

The TRIUMF M11 beam line was used for the tests [Fig. 1.17a]. Our tests used positively-charged electrons, muons, and pions, with momenta ranging from 140 to 350 MeV/c. In this momentum range, the particle identification separation between muons and pions is comparable to that between pions and kaons at the 2–3 GeV/c range relevant for Super$B$. The trigger and time-of-flight (TOF) system consisted of two scintillator counters, each with a pair of Burle micro-channel plate phototubes. The trigger rate was typically tens of Hertz, and the TOF resolution was 130 ps, providing clean separation between the particle species.

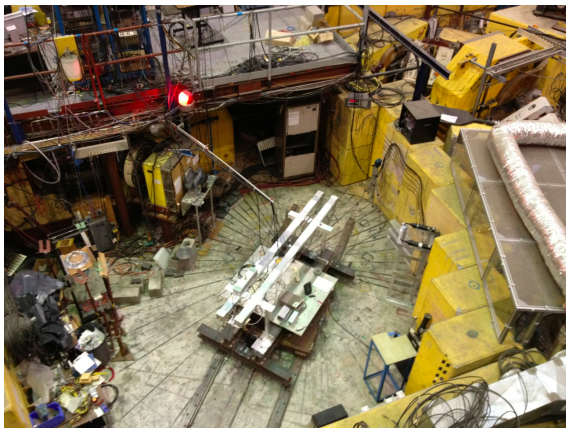

Figure 1.17: The M11 beam area at TRIUMF, showing two single-cell drift chamber prototypes under test in Summer 2012.

In the November 2011 test, the drift chamber waveforms were digitized using a CAEN switched-capacitor array, read out using the MIDAS data acquisition system. The bandwidth of this module is 300 MHz, which may be less than required for cluster counting, so in the Summer of 2012, a 4 GHz bandwidth LeCroy oscilloscope was instead used for digitization. In both cases, the amplifier and digitizer were connected by a 10 m long cable, the distance expected in the final design. Events were written to disk at 10–15 Hz. Figure 1.18 shows a typical waveform.

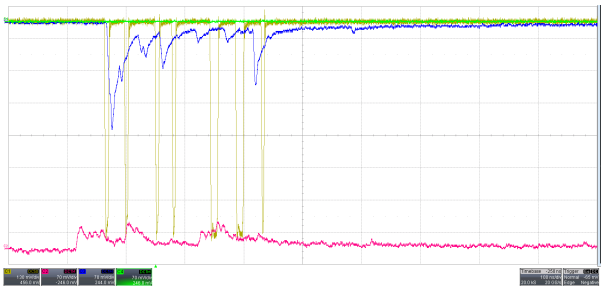

Figure 1.18: Waveforms recorded in Summer 2012 from a prototype with 20 μm sense wire (red) and 30 μm sense wire (blue), using two different 370Ω input impedance amplifier prototypes. The yellow curve shows the NIM logic signals from the time-of-flight system.

The benefits of cluster counting on particle ID performance are characterized by comparing the separation between muon and pion tracks using dE/dx only to the combination of dE/dx and cluster counting. Analysis is in progress, and results shown here are preliminary.

A track is formed by randomly selecting 40 samples of the same particle species as determined by the TOF system. The track dE/dx is obtained by discarding the largest 30% of the samples. Clusters are identified by a simple threshold on a smoothed version of the waveform. This algorithm is not necessarily optimal, and other methods are under study. Conversely, adequate performance may be achieved using a simpler algorithm that could be implemented in hardware, as opposed to an FPGA. The track is characterized by the average of the number of clusters in the 40 samples. The track dE/dx and cluster counting values are combined in a likelihood ratio that is used to label the track as a muon or pion. Figure 1.19 show examples of the results from the two beam tests. The addition of cluster counting significantly reduces the fraction of muons that are misidentified as pions.

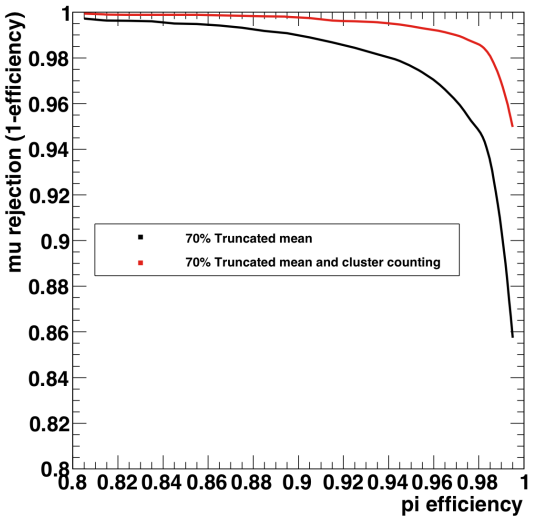

Figure 1.19: Fraction of muons identified as pions versus the fraction of pions satisfying the selection criteria, for dE/dx only, and for the combination of dE/dx and cluster counting. (Top) 140 MeV/c data, November 2011 test; (Bottom) 210 MeV/c data, summer 2012 test.

1.2.5.4 Aging studies

The goal of the aging studies is to establish that the proposed drift chamber can survive for a lifetime of at least 100 ab^{-1}.

These studies use an ^{55}Fe source both to age a test chamber, and to characterize its performance. The initial studies are using a 30 cm long chamber containing a single *BABAR*-like hexagonal-shaped cell, and an 80% helium 20% isobutane gas mixture. The sense wire is 20 micron gold-coated tungsten, and the field and bias wires are 120 micron gold-coated aluminum. The chamber is exposed to a 100 mCi ^{55}Fe source. The resulting current is monitored, along with temperature and atmospheric pressure, as a way to characterize gain as a function of accumulated charge. Once per week, the hot source is replaced with a low-intensity one and the pulse-height spectrum is recorded (Fig. 1.20). The location of the ^{55}Fe peak is an additional measurement of gain. The number of very small pulses is sensitive to the Malter effect, a form of aging of the field wires in which they accumulate an insulating coating. A second single-cell chamber, which is not exposed to the hot source, is used to calibrate out any possible gain effects due to gas variations, and to verify the gas density corrections. The chamber is operated at a voltage such that the electric field on the field wires is less than 20 kV/cm in order to minimize the Malter effect.

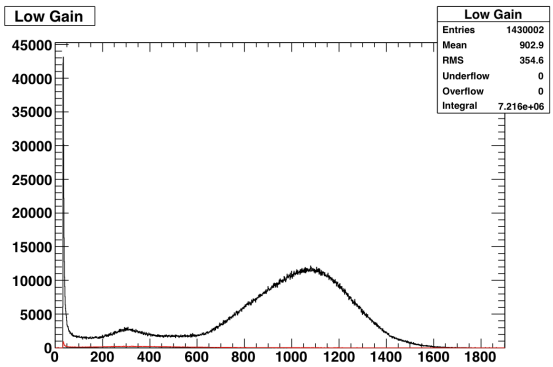

Figure 1.20: Pulse height spectrum recorded from an ^{55}Fe source by an aging chamber. The red curve is the underlying cosmic ray background.

The aging chamber shows a gain drop of 25% after accumulating 310 mC/cm over the last 20 months. This lifetime is significantly in excess of the 34 mC/cm accumulated by the *BABAR* drift chamber. The *BABAR* chamber saw a 10% loss of gain over that time.

The next aging chamber is currently under construction. It will include seven square cells, so that the central field wires are surrounded by sense wires, and will therefore accumulate the correct amount of charge (Fig. 1.21). It will use Super*B* materials, gold-coated 20 micron Molybdenum sense wires, and 80 or 90 micron bare aluminum field wires, and 90:10 helium-isobutane gas. The structure of the chamber will be aluminum, as for the current aging chamber, but the walls will be covered by samples of the carbon-fiber material that will be used in the actual chamber.

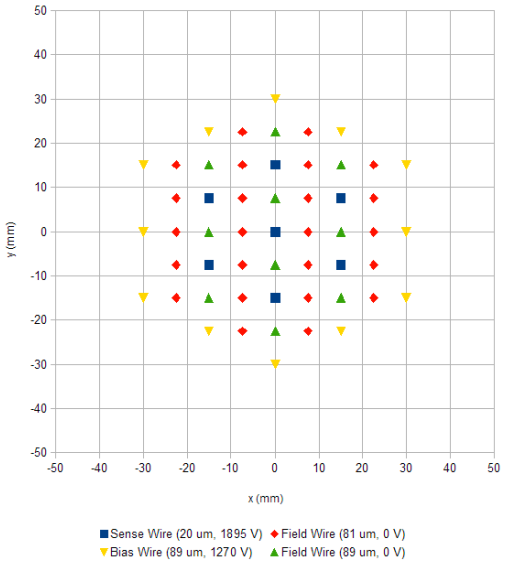

Figure 1.21: Wire layout of the new aging chamber under construction.

The amount of charge per cm expected for the Super*B* chamber is a function of the chamber occupancy, the gas gain, and the total running time. Current background calculations indicate occupancy levels comparable to *BABAR*, including a five-times safety factor. The Super*B* running time will also be comparable to *BABAR*. The gas gain may be higher, due to the requirements of cluster counting. The gas gain required is a function of the amplifier; the 50 ohm input impedance amplifier prototypes require four times the gas gain of the 370 ohm amplifiers, due to the impedance mismatch between the amplifier and the drift cell. The field wire diameter is, in turn, a function of the sense wire operating voltage, given the need to keep the electric field at the surface of the field wire below 20 kV/cm.

1.2.6 R&D Future Developments

At the time of this writing, a two week test beam data taking campaign has been completed with the full scale prototype (Prototype 2) at the M11 beam line in the TRIUMF laboratory, Canada. Data were collected with a beam of e,μ,π particles with momenta between 110 and 210 MeV/c.

The goal of this test is to reproduce and study in further details, with a more realistic full length, multiple cell prototype, the promising preliminary results on cluster counting and $\mathrm{d}E/\mathrm{d}x$ obtained with the single cell prototype described in Sec. 1.2.5.3. The analysis of these data has just started and will be the object of a future paper.

Another line of future development is centered in the realization of a prototype on-board feature extraction.

1.3 Mechanical Design

The drift chamber mechanical structure must sustain the wire load with small deformations, while at the same time be as light as possible to minimize the degradation of the performances of the surrounding detectors. The structure is also required to ensure tightness for the gas filling the drift volume. We opted for a structure entirely in Carbon Fiber (CF) composite, with an approximately cylindrical geometry. Given the studies shown in Subsec. 1.2.1.2, the active length of the chamber has been maximized. In particular the length in the backward direction is increased with respect to *BABAR* despite the 160 mm reserved in Super*B* for the possible backward EMC to be installed at a later stage; this is possible thanks to the new design of the drift chamber front-end electronics

(Sect.1.4), which require substantially less space than *BABAR*.

1.3.1 Endplates

The wires defining the cell layout are strung between the two endplates, which are required to:

a) sustain the total wire load of about 2 tons (see sec. 1.2.3) with minimal deformations;

b) be as transparent as possible to avoid degrading the performances of the forward calorimeter.

c) have 33,000 precisely machined holes to allow positioning the crimp feedthroughs with tolerances better than 50 μm;

The endplates are two identical pieces of 8 mm thick CF composite with inner radius of 270 mm and outer radius of 809 mm. Deformations under load can be minimized using a shaped profile. An optimization taking into account different constraints resulted in spherical convex endplates, with a radius of curvature of 2100 mm. Two CF stiffening rings (the outer one shown in Fig. 1.22) on the inner and outer rims help minimizing radial (axial) deformations. In the calculation an intermediate modulus carbon fiber (as T300, with a Young modulus of 45 GPa) was used. The 8 mm CF laminate is built using stacks of 250 μm plain weave plies with a $[0/45/45/0]_8$ structure. It was conservatively assumed that the average material characteristics are degraded by about 30 % or less after drilling the 33,000 holes on each endplate; detailed studies on this aspect will be performed on custom samples. The maximum displacements on the endplates is calculated to be less than 600 μm (Figure 1.23). As a comparison, the thickness of flat endplates to have such small deformations under the wire load would be 52 mm.

1.3.2 Inner cylinder

The drift chamber inner cylinder should be as transparent as possible to minimize the multiple scattering degradation to the p_T measurement. For this reason it was designed as a non-load-bearing structure: it must only guarantee gas tightness, and sustain possible differential pressures of about 20 mbar[2] between the inside and outside of the chamber. The 270 mm radius cylinder is composed by two 90 μm CF sheets sandwiching a 3 mm thick honeycomb structure to increase the moment of inertia and improve the buckling load. A 25 μm thick aluminum foil is glued on each CF skin for RF shielding. The possibility is being explored to build an even thinner inner cylinder, replacing the two 90 μm CF plies with two 50 μm Kapton foils. During the stringing phase the inner cylinder will be free

[2]The nominal differential pressure in normal operation of the Super*B* DCH will be 2 mbar or less, but the cylinder has been designed to sustain 20 mbar.

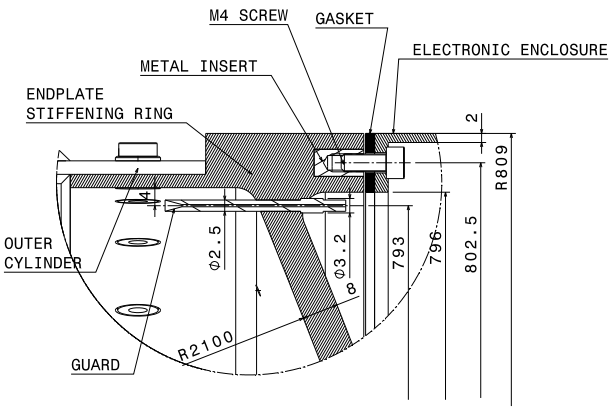

Figure 1.22: Detail of the outer flange of the DCH endplates.

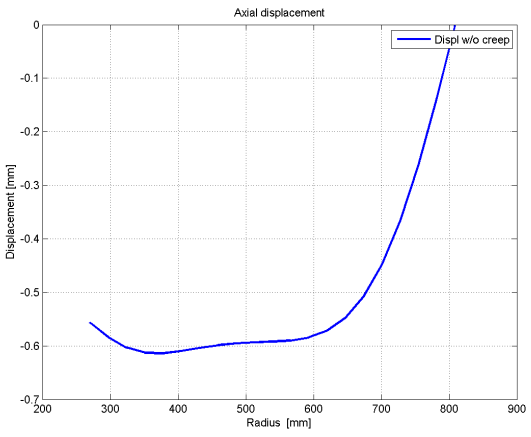

Figure 1.23: Displacement of each endplate due to the wire load.

to move longitudinally, being fixed only to one endplate. Only after stringing, when all endplate deformations are settled, will the cylinder be glued to the second endplate. A detail of the interface between the inner cylinder and the endplate is shown in Fig. 1.24.

1.3.3 Outer Cylinder

In addition to guaranteeing gas tightness and withstanding a differential pressure as the inner cylinder, the outer cylinder will also carry the entire wire load. It will be installed after completion of the wire stringing. To ease the construction and the mounting procedures, the cylinder is longitudinally divided in two half shells. Each shell consists of two 1 mm-thick CF skins laminated on a 6 mm-thick honeycomb core. A 25 μm thick aluminum foil is glued to each CF skin to ensure the RF shield. The sandwich structure guarantees a high bending stiffness and a high safety factor for global buckling.

1.3.4 Analysis of Buckling Instabilities

The buckling stability of the system was studied for all elements working under compression with the ANSYS Finite Element Analysis Program. Different methodologies were used for the main system elements, as described below.

1.3.4.1 Endplates

The results of a buckling linear analysis performed varying the endplate curvature radius are summarized in Table 1.4. The first buckling mode for the configuration with the nominal endplate curvature radius (2100 mm) is shown in Fig. 1.25. The nominal configuration with $R_{E.P.} = 2100$ mm is observed not only to minimize the displacement, but also to show the best buckling safety factor. We consider a safety factor above 10 adequate even after the uncertainties due to material imperfections and the effect of holes on the endplates are taken into account.

1.3.4.2 Inner Cylinder

A linear buckling analysis was carried out on the inner cylinder structure which, as discussed in Sect. 1.3.2, is only expected to sustain a gas overpressure of a few mbar. The first buckling modes of a perfect structure are shown in Fig. 1.26, for a very high load of 120mbar. It is well known that cylindrical thin shells are sensitive to geometrical imperfections. In order to realistically estimate the buckling safety factor, we have introduced such imperfections in our model, evaluating the critical load in each case with a non linear analysis. The results are shown in Fig. 1.27 and in Tab. 1.5: as expected, the larger the geometrical imperfections, the smaller the critical load. The table also shows that very small values are obtained when the inner cylinder is only made of two (0.09 thick) CF skins. The maximum load dramatically increases when a

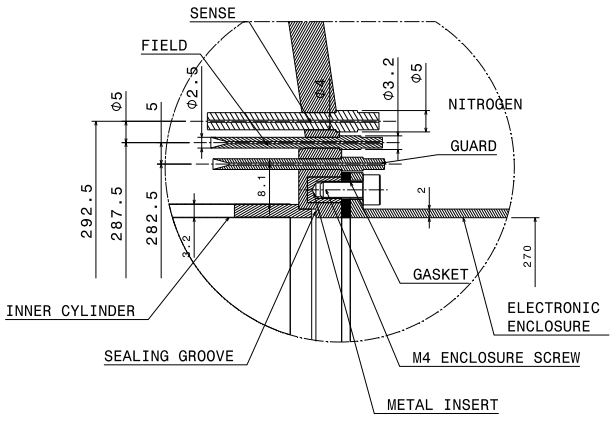

Figure 1.24: Coupling of the DCH inner cylinder to the endplate.

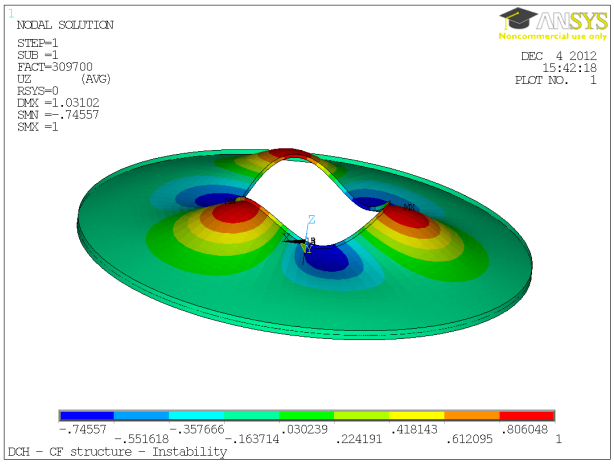

Figure 1.25: Calculated first buckling shape of the endplates.

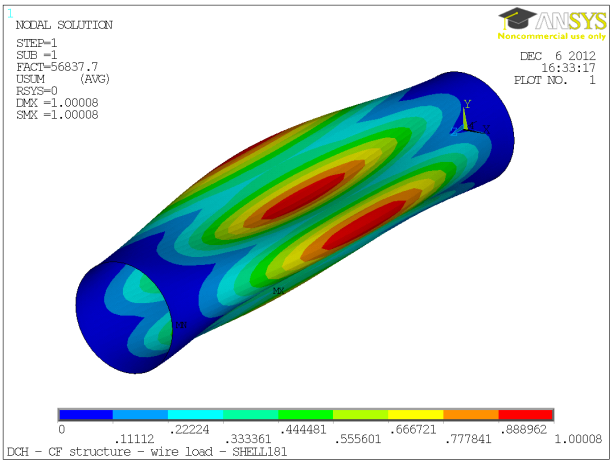

Figure 1.26: Calculated first buckling shape of the inner cylinder.

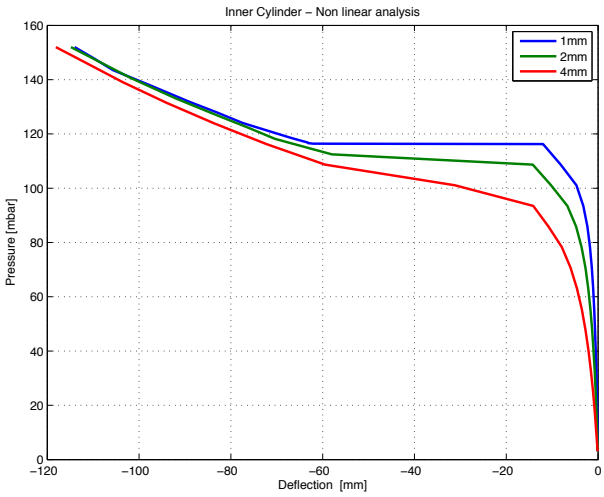

Figure 1.27: Inner cylinder critical load for different values of the geometrical imperfections.

Table 1.4: Maximum endplate deformations δ_{max}, static and buckling safety factors as a function of the endplate curvature radius $R_{E.P.}$.

$R_{E.P.}$ mm	Thickness [mm]	δ_{max} [mm]	Static S.F.	Buckling S.F.
2100	8	0.6	16.0	16.0
3000	8	1.1	12.4	8.0
4000	8	1.8	10.0	4.8

3 mm thick honeycomb structure is inserted between the CF skins. An acceptance threshold on the geometrical imperfections at the level of $2 \div 4$ mm can certainly be imposed, which leaves a reassuring factor 30 on the buckling load of the inner cylinder.

1.3.4.3 Outer Cylinder

A linear buckling analysis was performed on the outer load-bearing structure similarly to what discussed in the previous subsection. Also in this case geometrical imperfections were included, evaluating the safety factor under an axial load of about 21 kN.

These results are shown in Fig. 1.28 for the final structure (1CF 6HC 1CF) and summarized in Tab. 1.6 for different carbon fiber sandwiches.

1.3.5 Choice of wire

As described in Section 1.2.3, each cell has one sense wire surrounded by a rectangular grid of eight field wires. A smaller value for the sense wire diameter is generally preferred for several reasons: any given gas amplification, therefore electric field, can be reached with smaller applied high voltage; the avalanche starts closer to the wire, with smaller space-charge effects. In practice the wire diameter is limited by ease of handling, and by the mechanical resistance. For sense wires, we intend to use 20 μm Gold-plated Molybdenum wires. Molybdenum has lower resistivity than the more conventional W-Rh alloy, therefore smaller dispersion for pulses traveling along the wires. The

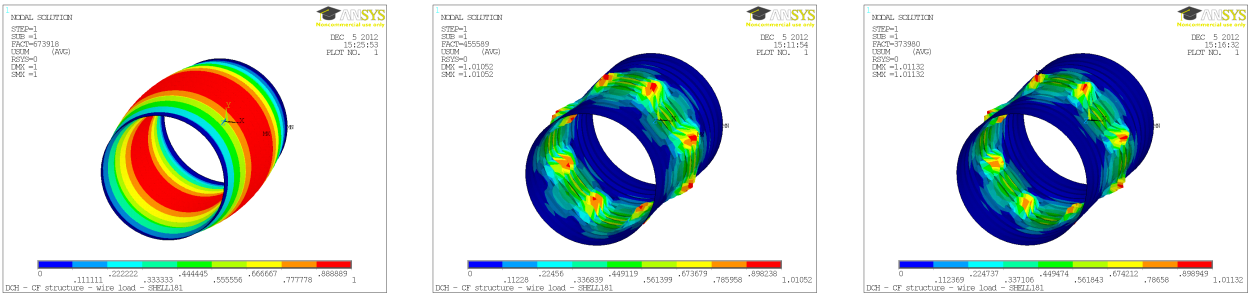

(a) No imperfections (b) 2 mm imperfections (c) 4 mm imperfections

Figure 1.28: Calculated outer cylinder 1^{st} buckling shape.

Table 1.5: Buckling load [mbar] as a function of the maximum size [mm] of geometrical imperfections in the inner cylinder.

Max. size [mm] / Config	0	1	2	4
0.09/0.09	0.84	0.74	0.68	0.56
0.09/3/0.09	120	108	99	86

Table 1.6: Outer cylinder safety factors for different thickness in mm of the Carbon Fiber (CF) and honeycomb (HC) components, and for different sizes of the geometrical imperfections.

Config	Nominal S.F.	2mm S.F.	4mm S.F.
2CF	24.0	10.8	8.0
1CF 3HC 1CF	22.0	12.8	8.3
1CF 4HC 1CF	33.6	13.5	9.0
1CF 6HC 1CF	33.6	22.8	18.6

density is also smaller than for Tungsten wires, resulting in slightly less tension (160 kg) on the endplates, and more importantly in less material in the tracking volume – the radiation length for all wires (field+sense+guard) increases from 4.25 cm with W-Rh wires to 6.95 cm with Mo wires, while X_0 for the wires and the 90%He – 10%iC_4H_{10} gas mixture increases from 480 m to 545 m. A mechanical tension of approximately 23 g will be applied to each wire, needed for it to show a gravitational sag of 200 μm. Such a tension is consistent with electrostatic stability and with the yield strength of the wire.

The field wires are chosen to be 90 μm diameter Al-5056 wires with a "stress-relieved" temper. The selected diameter keeps the electric field at the cathode surface below the limit of 20 kV/cm, considered a safe value in drift chambers not to trigger gas multiplication and help suppressing the Malter effect [**?**]. The temper considerably increases the wire tensile and yield strength, and reduces the loss of tension due to the creep effect. A nominal tension of 73 g will be needed to equalize the gravitational sag of sense and field wires (in the stringing phase the latter will be pulled at a slightly higher tension to compensate for the creep effect). Again, this tension is well within the elastic limit of the wires.

1.3.6 Feedthrough design

The feedthroughs locate the wires to within the specified tolerances, hold the wire tension, and, in the case of the sense wires, insulate against the high voltage. They must achieve these goals while maintaining a helium-tight gas seal.

A feedthrough is made from two components, a plastic outer insulator, and a conducting crimp pin (Fig. 1.29). The insulators are injection-molded parts formed from Celenex 3300-2, chosen for its low shrinkage during molding, dimensional stability, and high dielectric strength.

The crimp pins for the aluminum field wires are aluminum 6063. Studies are planned to determine whether copper or aluminum crimp pins are more suitable for the molybdenum sense wires. The crimp pins will have a gold-flash coating with a nickel underlayment.

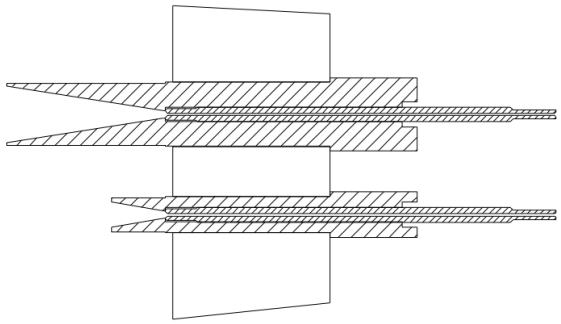

Figure 1.29: Sense wire (top) and field wire (bottom) feedthroughs from the *BABAR* drift chamber. The Super*B* parts will be similar.

The two parts are glued together with an epoxy that is dyed so that extraneous epoxy on the crimp pin can be identified and removed.

The tolerances are specified to ensure that the contribution to cell resolution is small, with tolerances on the sense wire parts significantly tighter than those on the field wires. Inner diameter of sense wire crimp pins at the wire release point will be 100 microns, and 200 microns for field wires. Concentricity of the pin hole with respect to the shaft diameter will be less than 30 microns, and eccentricity of the shaft will be less than 25 microns.

Each of the approximately 75000 feedthroughs will be individually tested against the specifications. Sense wire feedthroughs will have an additional test to verify HV performance.

1.3.7 Endplate systems

1.3.7.1 Electronics enclosures

The amplifiers mounted on the backward endplate of the drift chamber, and the high-voltage components mounted on the forward endplate are covered by the electronics enclosures. The volumes are filled with nitrogen to ensure that a leak of the flammable drift gas through the endplate cannot form an explosive mixture. The enclosures also protect the components inside, and provide the mounting points for the chamber as a whole.

The enclosures are light aluminum structures (Fig. 1.30). The main features are feedthroughs for the various signals and services used by the chamber: chamber gas, nitrogen, cooling water, amplifier power and signal, and high voltage. Each $1/16^{\text{th}}$ sector corresponds to approximately 500 signal cables, arranged into 8-channel ribbon cables and feedthroughs. These feedthroughs may also carry the power and control lines for each amplifier. The feedthroughs are mounted on removable panels, while the cooling lines are on the fixed ribs. The panels allow access for installation and repairs, although such accesses are expected to be rare. Although the endplates are curved, the panels can be flat, reflecting the geometries of the backwards calorimeter and the forward time-of-flight system on either side of the drift chamber. This will greatly simplify the necessary gas seals.

1.3.7.2 Cooling

The fast amplifiers mounted on the drift chamber endplates produce approximately 1200 W of heat. This heat must be removed to keep the temperature of the drift chamber and nearby detectors stable and uniform. The cooling system to accomplish this will be water based, operating at a pressure below atmospheric pressure. Small leaks will therefore cause air to leak into the water, rather than leading to water leaking into the electronics enclosure. The system is quite similar to one recently built for the near detector of the T2K experiment.

The major components of the system include two water reservoirs, one at atmospheric pressure, and the other maintained at an absolute pressure of 0.3 atmospheres; a pump to move water between the systems; cooling lines to the drift chamber and inside the electronics enclosures; valves and gauges; a heat exchanger that connects to the laboratory chilled water system; and a control system to maintain the desired water temperature. Appropriate corrosion in-

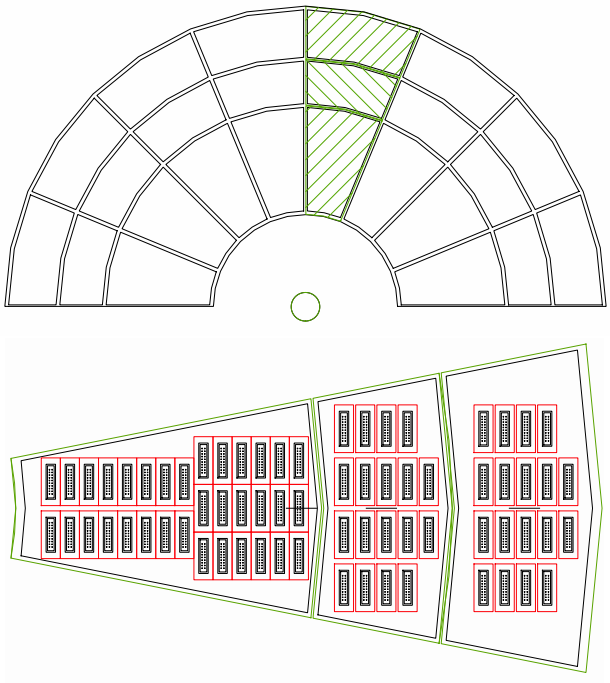

Figure 1.30: (a) The rib structure of each enclosure is machined from a solid piece of aluminum. (b) The feedthroughs are on panels mounted to the ribs.

hibitors and microbiocides will be added to the water. The lines within the enclosures will be mounted to the fixed ribs, and may include fins or other features to increase the surface area. These features, combined with turbulent nitrogen flow in the enclosure, may generate sufficient thermal flow from the amplifiers to keep the temperatures at an acceptable level. Mockups and thermal calculations will be undertaken to test this concept. The alternative will be cooling straps.

Although there is no heat generated on the forward endplate, cooling lines will be run to ensure a uniform temperature across the drift chamber.

1.3.7.3 Shielding

The aluminum structure of the electronics enclosures, together with the aluminum skins on the outer and inner cylinders, form a Faraday cage that encloses the amplifiers and the chamber wires. A 25 micron thick aluminum skin bonded to the endplates provides additional shielding between the chamber wires and the enclosure volumes.

1.3.7.4 Electromechanical boards

Electrical connections to the crimp pins are required at both ends of every wire. At the forward end, the HV distribution boards ground the field wires and provide HV to the sense wires via the circuit described in Sec. 1.5, and terminate the sense wire at the characteristic impedance of the cell. At the backwards end, service boards ground the field wires, and gather the signals from eight sense wires onto a single multi-conductor connector. The only active components on the service boards are the HV blocking capacitors.

Each of the ten superlayers requires a different size of HV distribution board and service board. Only a single style of 8-channel preamp card is required. Each board will service eight cells (four in radius by two in azimuth), typically corresponding to 32 crimp pins. A number of crimp pin connections much larger than this would make the board difficult to insert and remove.

The connections to the crimp pins are made using low-insertion-force connectors, such as the Hypertronics connectors used for *BABAR*. The details of how the curvature of the endplate is handled in the design of the cards will require prototypes and mockups.

Jumpers between adjacent boards will connect the ground planes. At the HV end, jumpers will distribute the HV among the typically three boards serviced by a single HV channel.

The endplate will include two blind holes per board that will be used with dowel pins to align the boards during insertion. We do not anticipate using pull-down screws, which would require a large number of tapped holes in the endplates. Each board will have two threaded holes that will be used to push against the endplate if it is necessary to remove the board. The boards will be removed rarely, if ever. One of the two holes will be used during normal operations to provide an electrical connection to the

aluminum RF shield on the endplate via a low-force spring connection.

1.3.8 Stringing

The chamber will be strung horizontally, with the inner cylinder in place (but not under load), and the outer cylinder absent. The wire load is held by a mechanical structure that attaches to the outer radius of each endplate and to a central shaft inserted through the inner cylinder. The chamber can be rotated about this shaft.

There will be two stringing shifts per day, five days per week. Each shift will have two teams consisting of two stringers plus a wire-transport robot. The robot is used to carry the wire between the endplates, reducing the chance of errors or damage to the previously strung wires, and keeping the interior of the chamber clean by eliminating the need for people to work in that area. The work will be done in a class 10000 or better clean room, with the interior of the chamber (including the robots and the previously strung wires) curtained off for greater cleanliness.

An abbreviated sequence of steps involved in stringing a wire is:

- A stringer attaches the wire to a steel needle and inserts it through a plastic sleeve into the appropriate feedthrough hole, where it is captured by the magnetic head of the robot.

- The robot carries the wire to the other endplate, where the needle is taken by the second stringer, who pulls the additional wire needed. The robot moves into position for the next wire when the second stringer indicates that they have finished pulling the wire. Both ends of the wire are then placed in wire holders before being cut.

- Each stringer feeds the wire through a feedthrough, places a ring of glue around the shaft of the feedthrough, and inserts it in the hole. The glue will be thixotropic gel cyanoacrylate adhesive such as Loctite 454 or 455, dyed red for ease of inspection.

- The second stringer crimps her crimp pin using a foot-operated pneumatic tool, such as the Simonds MSP-1 Squeeze Pliers. The first stringer then applies the appropriate tension using a pulley and weight, and crimps her crimp pin. Because the deflection of the endplate is negligible under the wire load (Fig. 1.23), wires can be tensioned at their nominal values. Excess wire is cut at both ends, leaving 1 mm protruding for inspection purposes.

- Once both teams have finished ten wires, the chamber is rotated into position for the next set of ten.

The third shift each day is used for quality control. The steps include measuring the tension, visually inspecting the glue seals around the feedthroughs, looking for excess glue on crimp pins, and straightening bent crimp pins. Wire that have tension out of tolerance (a gravitational sag more than 15 microns from nominal) are removed, and the holes cleaned. These wires are restrung at the start of the next stringing shift. The third shift also makes the gas seal between the wire and crimp pin using a low-viscosity cyanoacrylate adhesive such as Loctite 493, dyed red for easier inspection.

One stringer starts work an hour before the others to prepare the glues, lay out the parts needed that day, and to verify that all crimp tools are producing crimps of the correct size.

Each team is expected to complete 80–100 wires per shift, for a total of approximately 350 per day.

1.4 Electronics

1.4.1 Design Goals

The Super*B* Drift Chamber front-end electronics is designed to extract and process approximately 8000 sense wire signals to:

- measure the electrons drift times to characterize a track (momentum of charged particles)

- measure the energy loss of particles per unit length, dE/dx (particle identification)
- provide hit information to the trigger system (trigger primitives)

Two methods will be discussed for the energy loss measurements. We first present a solution already widely used in existing drift chambers, based on the measurement of the integrated charge on each sense wire, discarding the largest charge values to remove the Landau tails (standard readout). Then we present the baseline of our choice, which is based on the counting of the primary ionization clusters (Cluster Counting), which has never been used in a large scale drift chamber before. Because the front-end requirements for the two options are quite different, we shall discuss them in separate sections.

1.4.2 Standard Readout

1.4.2.1 Charge measurement

The method is based on an integrated charge measurement, which allows the use of relatively low bandwidth preamplifiers. This makes the front-end chain less sensitive to noise pickup and instabilities, a required condition in a system with a large number of channels.
The three main specifications for a charge measurement are: resolution, dynamic range and linearity.

- *Resolution*

The goal of a charge measurement to be used for particle identification is to determine the most probable energy loss per unit length to a precision of the order of 7.5%. This can be achieved, despite the large fluctuations present the ionization process, by sampling the collected charge many times (once per DCH hit cell) and by applying the "truncated mean" method to obtain the peak value of the resulting distribution to a precision of several percent.
The Super$B$ drift chamber design parameters and expected working conditions aim at obtaining an overall single cell energy loss resolution (σ_E) of about $25-30\%$, mainly driven by the detector contribution. To make the contribution of the front-end electronics σ_{EL} negligible, we set a limit at $\sigma_{EL} \leq \sim 5\%$. Finally, if we assume that the charge collection due to a minimum ionizing particle crossing orthogonally the cell is about 50 fC ($\sim 2fC/e$ @ 10^5 nominal gas gain), we can infer a limit to the Equivalent Noise Charge (ENC) for a single front-end channel of about $50\ fC \cdot 0.05 \simeq 2.5\ fC$.

- *Dynamic range*

With 8 bits ADCs the dynamic range is $2.5-500\ fC$. This is more than enough to satisfy the system requirements.

- *Linearity*

As stated above, a single cell energy resolution is about $25-30\%$. Therfore, a linearity of the order of 2% largely satisfies the system requirements.

1.4.2.2 Time measurement

As for the charge measurement, we have three main specifications: resolution, dynamic range and linearity.

- *Resolution*

One of the Super$B$ drift chamber requirements is the charged particle tracks reconstruction. The measurement consists of recording the arrival time at the sense wire of the first ionized electron. The spatial resolution (σ_S) is strictly related to the time resolution and gets contributions from primary ionization statistics, electrons diffusion time and time measurement accuracy. To achieve the required point resolution of $\sigma_S \sim 110\mu m$, and assuming that the first two effects account for about 100 μm, the upper limit for the electronic contribution can be deduced to be $\sigma_{EL} \leq \sim 50\ \mu m$. Because helium based gas mixtures are characterized by a non saturated drift velocity up to high fields [5], this velocity rapidly increases as the electrons approach the sense wire. A value of 2.5 $cm/\mu s$ (25 $\mu m/ns$) [6] has been used to evaluate the maximum acceptable error in a time measurement, that is $\sigma_t \leq 50[\mu m]/25[\mu m/ns] \simeq 2\ ns$.
Discarding the bunch length contribution

(tenths of ps), there are two main error sources in time measurements: the discriminator jitter and the TDC resolution (digitization noise). The discriminator jitter, in turn, has two main contributions: signal noise and time-walk.
The signal noise contribution is generally small and can be evaluated according to $\Delta t = \sigma_{noise}/(dV/dt) \simeq \sigma_{noise} \cdot \tau/V_{max}$ where τ is the preamplifier-shaper peaking time. Assuming that a single electron cluster generates a signal of amplitude $\sim 20\ mV$, and that the noise and the peaking time associated with the signal are $\sigma_{noise} \sim 3\ mV(rms)$ and $\tau \sim 5\ ns$, we get a noise contribution to the time resolution of about 0.8 ns.
The time-walk effect is caused by the signal amplitude variation. With a peaking time of about 5 ns, a time-walk contribution for a low-threshold leading-edge discriminator can be estimated to be about 1.5 ns.
Finally, the digitization noise depends on the digitization unit Δ according to the formula $\sigma = \Delta/\sqrt{(12)}$. Using $\Delta \simeq 1.5\ ns$ a digitizing noise of about 0.45 ns is obtained.
In summary, without corrections, the time resolution is dominated by time-slewing effects. It can thus be estimated to be about 1.8 ns (including all contributions). Nevertheless corrections can be applied using digitized signals to minimize time-slewing effects thereby reducing the time walk contribution (Fig. **??**).

- *Dynamic range*

The TDC range depends on the drift velocity and on the cell size. A maximum drift time of about 600 ns has been estimated for Super$B$ drift chamber cells. Providing some safety factor, a TDC range of about 1 μs is enough to include any jitter in trigger generation and distribution.

- *Linearity*

A linearity of the order of 1% fully satisfies time measurement requirements.

1.4.2.3 Front End Electronics

The drift chamber FEE chain (Fig. **??**) is split in two blocks: on-detector and off-detector electronics. In the following paragraphs we will give a description of the on-detector electronics while the description of the Off Detector Electronics can be found in Sec. **??**.

- *On Detector Electronics*

Preamplifier boards will contain HV blocking capacitors, protection networks, preamplifiers and (possibly) shapers-amplifiers. Because of the small cell dimensions, many cells can be grouped in a single, multi-channel preamplifier-shaper board. Signals and power supply cables will be connected to the boards by means of suitable connectors.
In addition to the requirements on the Signal to Noise Ratio (SNR), each preamplifier should be characterized by enough bandwidth to preserve signal time information meeting the power requirement of not more than $20 - 30\ mW$ per channel, to limit the total power dissipation on the backward end-plate to $160 - 240\ W$. This will allow the use of a simpler and safer forced-air based cooling system (no risk of leak).
Concerning the circuit implementation, since the channel density is low and a simple circuit can be used, an approach based on SMT technology can be adopted thus avoiding a specially designed (and expensive) ASIC development.

Table 1.7: Preamplifier main specifications

Linearity	$< 2\%(1 - 100fC)$
Output Signal Umbalance	$< 2\%(1 - 100fC)$
Gain (Differential)	$\sim$ 5.2 mV/fC
Z_{IN}	110 Ω
Z_{OUT}	50 Ω
Rise time	$\sim$ 2 ns ($C_D = 24pF$)
Fall time	$\sim$ 13 ns ($C_D = 24pF$)
Noise	1350 erms ($C_D = 24pF$)
V_{SUPPLY}	4V
P_D	$\sim$ 30mW

As an example, the simulation of a three stages transimpedance preamplifier based on SiGe transistors has been carried out. The first stage dominant pole is around 26 MHz while other stages have been designed with wider bandwidth thus resulting in a good separation in terms of cutoff frequencies.The simulation results are given in table 1.7 while Fig. 1.31 shows the (simulated) output waveforms for 3 differ-

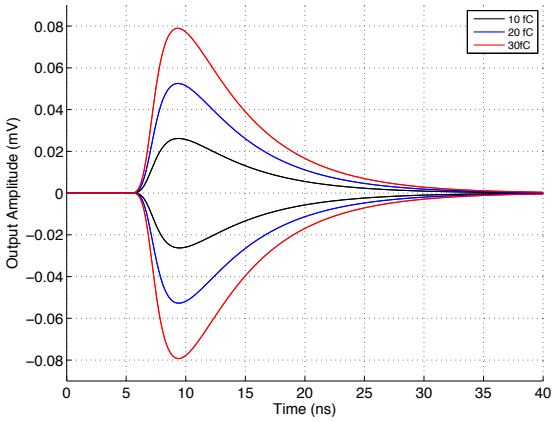

Figure 1.31: Preamplifier output for a 10, 20 and 30 fC test pulse ($C_{DET} = 24\ pF$)

ent input charges (10, 20 and 30 fC) injected through the test input.

1.4.3 Cluster Counting

The cluster counting technique is very powerful as it leads to an improved particles identification. To fully exploit the technique, individual ionization clusters must be identified.

In our system we use slow drift gas mixtures ($\sim$1 $\mu s/cm$), state of the art high sampling frequency digitizers (at least 1 GSPS) and fast processing (data throughput must sustain the Super$B$ expected 150 kHz average trigger rate). These modules require a large amount of power, forcing us to limit the number of channels to 8-16 channels per Amplifier Digitizing Board (ADB).
Moreover, fast amplifiers must be used on the preamplifier boards, which results in a larger power requirement than that of the standard readout. As a consequence, we are considering the use of a local liquid cooling system. The wide bandwidth requirement also impacts on the type of cables used to interconnect the preamplifiers with the ADBs and on the noise pick-up sensitivity of the full system .
In addition, the use of cluster counting requires that the signal reflection in the sense wires be eliminated. This is done by mean of termination resistors (R_T), which results in a lower limit on the system intrinsic noise.

Provided the cluster detection efficiency is sufficiently high, information from the cluster counting measurements can be used for tracking purposes. This requires storing the time of arrival at the sense wires of all the clusters, instead of simply counting them.
Specifications for the cluster counting measurements, as for the standard readout, must be given on resolution, dynamic range and linearity.

- *Resolution*

The resolution of the digitizers depends on the lowest signal amplitude to be sampled and the system baseline noise. Assuming an average input signal of $\sim 6fC/e$ @ $3 \cdot 10^5$ gas gain, a preamplifier-shaper gain of $10mV/fC$ and a safety factor of 2 to account for gas gain fluctuations, the average cluster signal is about 30 mV for a single electron.
We can estimate the preamplifier ENC from that of the dominant noise source, that is the termination resistor. Assuming a $CR - RC$ shaping circuit and a 3 ns peaking time, we get an ENC of about 0.2 fC, that is about 2 mV rms for a preamplifier gain of 10 mV/fC. Thus a voltage resolution of about 2 mV allows good control of the system noise and of the cluster signals reconstruction.

- *Dynamic range*

The cluster counting method requires the observation of peaks (corresponding to the clusters) in the digitized signals. An upper limit of the signal dynamic range (discarding gas fluctuations) is then given by the expected total ionization. Helium based gas mixture have already been well characterized [7]. We can assume that a minimum ionizing particle (m.i.p.) crossing orthogonally a 1.2 cm square cell filled with a $90\%\mathrm{He} - 10\% i\mathrm{C_4H_{10}}$ gas mixture, will generate on average about 22 electrons. Thus the dynamic range of an 8 bits ADC is fully adequate for cluster counting measurements.

- *Linearity*

As we are interested in finding (and tagging) signal peaks, a linearity of 2% fully satisfies the requirements.

1.4.3.1 Front End Electronics

The drift chamber FEE chain for cluster counting is similar to that for the standard readout. In this scenario, the electronics modules will be connected with mini coaxial cables. Because of the smaller number of channels per ADB, both the number of crates and ADBs will increases significantly (tables **??** and **??**).

- *On Detector Electronics*

Because preamplifier boards will host high bandwidth ($\sim$ 350 MHz) amplifiers, the layout and assembly are more difficult compared to the standard readout scenario. Particularly, special attention must be provided to avoid ground loops to minimize instabilities and external noise pickup.
The baseline solution foresees the use of commercially available fast transimpedance amplifiers. Anyway the design of a preamplifier based on high bandwidth and low-noise SiGe SMT transistors will be investigated as well.

1.5 High Voltage system

1.5.1 Main System and HV Distribution Boards

The high voltage distribution network will be located on the forward end-plate. The distribution board modularity will match the preamplifier modularity while the number of distribution boards connected to a single HV channel will depend on the layer (example: inner layers = 2 boards, outer layers = 5 boards).

The HV distribution system consists of power supplies and distribution boards, along with associated cables, feedthroughs into the forward electronics enclosure volume and HV distribution within that volume. The voltage will be supplied by a CAEN SY4527 Universal Multichannel System supply with 16 A1535N distribution boards, giving a total of 384 channels. This is sufficient granularity that a single channel failure will have a very small impact on detector performance. Spares of both the SY4527 and the A1535N will be available. The A1535N permits individual channels to operate in current-generator mode in case of overcurrents. This feature was found to be extremely useful for the *BABAR* drift chamber as it permitted the chamber to handle locally high background rates without ramping down the chamber HV.

Individual HV channels are brought to the drift chamber from the A1535N boards via multistrand cables with A996 52 pin Radiall connectors at both ends.

The multiconductor cable connects to a filter box containing a low-pass filter, located at the inner radius of the forward enclosure. The individual channels are fanned out within the enclosure to the HV distribution boards (Sec. 1.3.7). Each HV channel supplies two or three 8-channel distribution boards, depending on the superlayer.

The HV distribution and sense wire termination circuit is shown in Fig. 1.32. If termination is not used, the termination resistor (R_T) and the 500 pF capacitor per sense wire are removed.

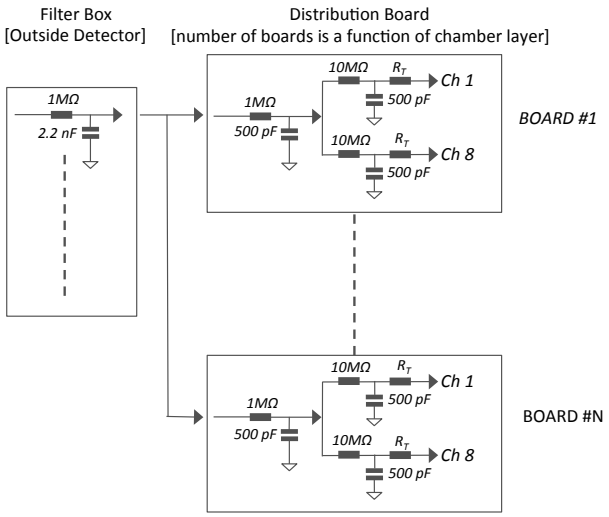

Figure 1.32: HV distribution network.

1.6 Gas system

The drift chamber is filled with a gas mixture of 90% helium and 10% isobutane. The gas system supplies the appropriate gas mixture to the chamber, while maintaining the required flow rate, pressure, purity, and composition stability. It includes safety items such as flammable gas sensors and release valves to protect the gas system, detector, and personnel from dangerous conditions caused by component failures or operator errors. To reduce the operating costs, 85% of the gas will be purified and recirculated.

The mixing will be done using mass flow controllers that will maintain the isobutane fraction at $(10.0 \pm 0.1)\%$. A parallel set of rotameters may be included to allow for high flow rate flushing. The system will allow a fraction of the flow to pass through a temperature-controlled water bath, which will be used if we decided to add water to help control the symptoms of aging.

The gas composition is verified using a set of analyzers to measure isobutane, oxygen, and water. The analyzer set will be able to sample gas at a variety of points in the gas system, such as before or after the gas enters the chamber or the filters.

This will be a recirculating gas system, which reduces operating costs and air pollution from the isobutane. The total flow will be 15 liters per minute, of which 2.5 liters per minute will be fresh gas. For a chamber volume of 5000 liters, this corresponds to four volume changes per day, or one volume of fresh gas every 1.5 days. The flow is controlled by an explosion-proof compressor, which is regulated to maintain a chamber pressure of 4.00 ± 0.05 mbar (0.4% of an atmosphere) above atmospheric pressure.

The primary gas lines between the gas mixing station and the detector will be welded and pressure-tested stainless pipe, 1.5 inches diameter. This will be reduced to 0.75 inch diameter in the cable trays through the detector. The input line is fanned out to 8 lines of 5 mm diameter on the rear endplate, while the output line is fanned out to 16 lines of 5 mm diameter on the forward endplate.

The gas returning from the detector passes through a palladium catalytic filter which removes oxygen by the reaction $13O_2 + 2C_4H_{10} \rightarrow 8CO_2 + 10H_2O$. The resulting water is removed by an alumino-silicate molecular sieve. The system contains two such sieves, so that one can be regenerated (i.e., have the absorbed water removed) by flushing with helium at elevated temperature without stopping operations. This filter system was originally built for the *BABAR* drift chamber and will be reused for Super$B$.

The gas temperature and pressure will be monitored at various points in the system, along with atmospheric pressure. These quantities will be used to calculate gain correction due to gas density. We will also monitor gas gain using a small, single-cell chamber that will be mounted on the return line from the chamber. Any variations in the current induced by an ^{55}Fe source after applying the density correction would indicate gain variations due to gas composition or chamber aging.

The majority of the gas system components will be in the gas hut (or room), which will be located at an exterior wall of the interaction hall. Two additional racks close to the detector will contain bubblers, pressure sensors, and valves. The gas storage areas will be outside, under cover, immediately adjacent to the hut. The isobutane, since it is flammable, will be stored in a physically separate area from the other gases. The isobutane tanks and lines will be heated and insulated.

The gas system includes an extensive safety system to protect personnel and equipment. This system will be reviewed and approved by the laboratory. Aspects of the safety system include:

- ventilation in the gas hut, which, when combined with flow restrictors on the lines into the hut, ensure that a leak cannot create an asphyxiation hazard.

- nitrogen flows in the exhaust lines and into the electronics enclosures on both endplates.
- flammable gas sensors in the gas hut and the bubbler rack.
- an oxygen sensor on the return line.
- bubblers and redundant pressure sensors to protect the chamber against over pressure.
- an independent helium line and regulator to protect the chamber against subatmospheric pressures.
- administrative controls on changes to the gas system.

The system is designed such that it will remain safe even during extended power outages. We will undertake regular maintenance and keep sufficient spare parts to ensure reliable operations.

1.7 Monitoring and Calibration

1.7.1 Monitoring

Environmental and systems-related parameters that are potentially time dependent will be continuously monitored while Super$B$ is taking data. These will be collected asynchronously from the e^+e^- collision data stream within the experiment's "slow controls" system. The parameters will be redundently monitored and include:

- temperature: four in the experimental hall; four on the outside of each gas enclosure bulkhead; four inside the gas enclosure at each end
- pressure: two in the experimental hall; two in each gas enclosure volume
- high voltage and current (read for each HV card)
- high voltage crate voltages, currents and temperatures (read for each HV card)
- preamplifier low voltage and current (read for each read-out board)
- digital electronics voltages, currents and temperature (read for each crate)
- discriminator levels set for cluster counting either in the FPGA or local derivative discriminator (one per channel)
- oxygen, helium, isobutane and H_2O concentrations in the gas system at the input and output lines of the drift chamber
- average ^{55}Fe pulse heights from two gas quality monitoring chambers, one on the input the other on the output gas line of the drift chamber
- cooling system monitors: temperature and pressure on the input and output lines and immediately before and after the chamber

The quantities will be averaged over each minute and made available to the data-taking shift crew and drift chamber experts in the form of digital "strip charts". These will be actively monitored by specialized software and stored in a database for future examination. The annual data volume will, at most, be a few Gigabytes. The active monitoring will read the quantities and determine if a quantity is outside tolerance. If a monitored quantity falls outside its tolerance band, the shift crew will be alerted by an alarm alerting them to the need for action.

The gas quality will be monitored using the pulse height information from the ^{55}Fe source in the two monitoring chambers. Problems with the gas mixture will be revealed by changes in the gas gain after correcting for expected changes in gas density associated with atmospheric pressure, or perhaps experimental hall temperature, changes.

In addition to these environmental and systems-related parameters, the drift chamber will be actively monitored to ensure that it is operating properly. Histograms of the number of hits per cell integrated over 10 minuutes for High Level Trigger events will provide on the order of 10^3 hits per cell for an event rate of 25 kHz

(based on the High Level Trigger accepting a cross-section of about 25 nb for the $10^{36}\mathrm{cm}^{-2}\mathrm{s}^{-1}$ design luminosity). This will provide the ability to monitor if any given cell's occupancy deviates by more than about 10% from from nominal every ten minutes. In addition, histograms of the number of hits per layer can be used to monitor if a drift chamber layer's occupancy deviates by more than a percent every minute. Specialized software will alert the shift crew if cell and layer occupancies fall outside tolerances. Trigger rates for triggers using the drift chamber will also be monitored and used to establish that the drift chamber is operating as expected.

The monitoring of some quantities made available by the online reconstruction, such as D^0 and K^0_S mass peaks, m_{es}, and $\Delta\mathrm{E}$ will also be used to validate drift chamber operational integrity.

1.7.2 Calibration

The time-to-distance relations will be calibrated initially with cosmic ray muons. Each cell will have its own calibration, although cells with a common electrostatic configuration are expected to have the same time-to-distance parameters. Comparisons of parameters of those families of cells will provide a measure of quality assurance of the calibration process.

When beams are colliding, low multiplicity physics events, such as $\mathrm{e}^+\mathrm{e}^- \to \mu^+\mu^-$ and Bhabha events, will be used to calibrate the time-to-distance relations and the calibrations will be continuusly updated at a rate determined by the luminosity. The $\mathrm{d}E/\mathrm{d}x$ calibrations will use physics events in which kinematics provide a cleanly identified particle. For example, $\phi \to K^+K^-$, $K^0_S \to \pi^+\pi^-$, and $D^{*+} \to K^+D^0$,$D^0 \to K^-\pi^+$ can be used to select kaons and pions; and $\Lambda \to p\pi^-$ can be used to select protons. Control samples of leptons for particle identification calibration are provided by $\mathrm{e}^+\mathrm{e}^- \to \mu^+\mu^-\gamma$ and $\mathrm{e}^+\mathrm{e}^- \to \mathrm{e}^+\mathrm{e}^-\gamma$ events. These same control samples will be used to calibrate the optimal parameters in the cluster counting algorithm used for particle identification.

1.8 Integration

1.8.1 Overall geometry and mechanical support

The envelope of the drift chamber is determined by the tungsten shield and the DIRC at the inner and outer radii, and by the backward calorimeter and the FTOF in the negative and positive z directions. There are 5 mm radial clearances between the drift chamber and the surrounding components, and 5 mm clearance between the drift chamber envelope and the backward calorimeter. The FTOF is directly mounted onto the drift chamber. The envelope in the backward direction includes the space occupied by the signal cables after they exit the enclosure.

In *BABAR*, the chamber was supported at the backward end by turnbuckles connected to the inner surface of the DIRC central support tube (CST). We envision using a similar system, although the actual mounting points used by *BABAR* will be obscured by the backward calorimeter.

In the forward direction, the drift chamber and FTOF form an integrated mechanical package supported by the CST. Figure 1.33 shows the mounting components used by the *BABAR* drift chamber. Note that the support point on the DIRC is on the z end surface of the CST, not the inner radius. Because the Super$B$ chamber is shorter in the forward direction than *BABAR*, the corresponding support tabs will be on the FTOF, not the chamber.

1.8.2 Installation and alignment

The chamber and FTOF will be installed prior to the forward and backward calorimeters and the tungsten shielding. The installation will reuse the existing *BABAR* equipment, which is currently stored at SLAC. The chamber is supported at the inner radius and slid along a supporting beam that passes through the inner cylinder (Fig. 1.34).

Both forward and backward enclosures will contain a number of precision 6 mm dowel holes

Figure 1.33: Mechanical mounting points for the *BABAR* dch on the (a) forward and (b) backward ends. Both ends are attached to the DIRC central support tube.

into which target holders for corner-cube reflectors can be mounted. The enclosures in turn are doweled to precise reference holes on the endplates, referencing the target locations to the sense wire locations.

The mounting systems at both ends allow for several mm of adjustment in x and y. The chamber location will be adjusted to center the chamber in x and y on the interaction point and to align the sense wire direction with the magnetic field. The tolerances on these alignments have not yet been specified. The mounting system fixes the chamber location in z at the forward end, but permits a small amount of motion at the backwards end in case of relative thermal

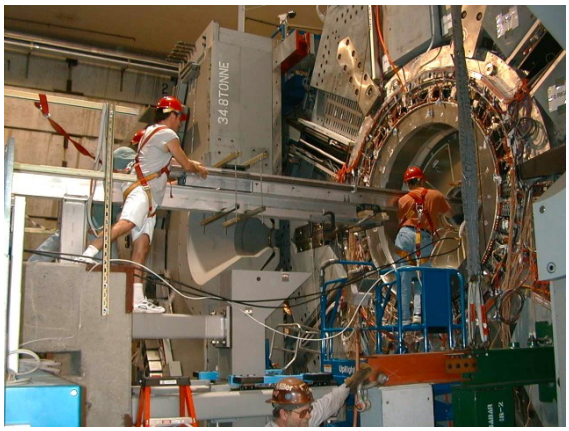

Figure 1.34: *BABAR* drift chamber during installation. The same tooling is available for use by Super$B$.

expansion. The tolerance on the location in z will be significantly looser than those on x and y.

1.8.3 Services

The services required for the backward end are listed below. These will reach the backward enclosure via 16 slots in the outer radius of the steel plug located within the DIRC strong tube. Each slot will be approximately 50 mm in radius by 250 mm wide. Cables continuing to the digitizing crates, located on the top of the detector, will be routed to wireways at the end of the IFR iron immediately after exiting the DIRC strong tube.

Note that within the radial extent of the backward calorimeter, the signal cables (and all other services) are routed to stay within the drift chamber envelope.

- Signal cables: approximately 8000 coaxial cables, RG-179, 2.54 mm in diameter, organized into 8-cable ribbons. These are 10 m in length, and travel to the digitizing electronics crates.

- Calibration cables: RG-179, one for every eight signal channels. Also originate at the digitizer crates.

- Low-voltage power: Four 1/0 welding cables, 14.7 mm diameter. Originate in the electronics hut.
- Cooling lines: 16 lines (8 separate circuits, each with a supply and a return line), 26.2 mm reinforced PVC. The sub-atmospheric water-based cooling system (Sec. 1.3.7) will be close to the detector, but outside of the radiation area.
- Drift gas: one line, 19 mm diameter stainless steel. Originates in the gas hut. This line increases to 38 mm diameter after exiting the detector.
- Nitrogen flush gas: two lines, 19 mm diameter stainless steel. Also from the gas hut.

The services for the forward end will exit the detector in the radial space between the tungsten shield and the FCAL. The services for the forward region are:

- High voltage: 16 56-conductor cables, 14 mm diameter. Originate at the HV supplies in the electronics hut.
- Drift gas: one line, 19 mm diameter stainless steel. Originates in the gas hut. This line increases to 38 mm diameter after exiting the detector.
- Nitrogen flush gas: two lines, 19 mm diameter stainless steel. From the gas hut.
- Cooling lines: 2 lines, 19 mm reinforced PVC. From the cooling system.

1.9 Bibliography

[1] B. Aubert *et al.* (*BABAR* Collaboration), *The BABAR Detector*, Nucl. Instrum. Methods Phys. Res., Sect. A **479**, 1 (2002).

[2] R. Veenhof, *Garfield - simulation of gaseous detectors* CERN-W5050, Version 9.

[3] CLEO reference.

[4] M. Adinolfi *et al.* (KLOE Collaboration), *The tracking detector of the KLOE experiment*, Nucl. Instrum. Methods Phys. Res., Sect. A **488**, 51 (2002).

[5] A. Sharma, F. Sauli, Nucl. Instr. and Meth. A 350 (1994) 470.

[6] C. Avanzini et Al. Nuclear Instruments and Methods in Physics Research A449 (2000). 237-247.

[7] P.R.Burchat and John Hiser Studies of helium gas mixtures in drift chambers SLAC-PUB-5626 SCIPP 91/25 September 1991.